scientific reports

Check for updates

OPEN

Computational identification and evaluation of novel PD-L1 inhibitors for cancer immunotherapy

Hina Manzoor[1], Muhammad Umer Khan[1]✉, Chaudhry Ahmed Shabbir[2], Raima Rehman[3], Alaa S. Alhegaili[4], Muhammad Ikram Ullah[5], Heba Bassiony Ghanem[5] & Ayman Ali Mohammed Alameen[5]

Antibody-based therapies targeting the PD-1/PD-L1 pathway have shown promise in anticancer immunotherapy; however, challenges such as high cost, immunogenicity, and limited penetration highlight the need for small-molecule inhibitors. To find new inhibitors, this study used the ligand found in PD-L1 (PDB ID: 7DY7) as a reference for virtual screening. The co-crystallized HOU inhibitor and selected ligands binding to the PD-L1 active site were assessed using Maestro 12.5 molecular docking and molecular dynamics (MD) simulations. The top ligands were evaluated for pharmacokinetics through ADMET profiling and chemical stability using Density Functional Theory (DFT). With a docking score of − 8.512 kcal/mol, Lig_1 demonstrated the greatest binding, establishing hydrogen bonds with the important residues of PD-L1, generating stable hydrophobic contacts, and π–π stacking with Tyr56. Because Lig_1 has better pharmacokinetic characteristics than CCL, especially its capacity to cross the blood–brain barrier (BBB), it has become a prospective contender. With negligible structural fluctuations, supported by RMSD and Radius of Gyration (Rg) studies, a 100-ns MD simulation further confirmed the steady binding of Lig_1. Lig_1 ensures persistent PD-L1 engagement by maintaining strong hydrophobic contacts and π–π stacking with Tyr56. These results showed the potential of Lig_1 as a new PD-L1 inhibitor by showing that, like CCL, it may cause PD-L1 degradation and interfere with PD-1/PD-L1 signaling. This study offers critical insights into the design of next-generation small-molecule inhibitors, paving the way for more effective cancer immunotherapies.

Keywords Cancer, Immunotherapy, PD-L1, LBVS, Molecular docking, Molecular dynamics

In 1863, Virchow observed leukocytes infiltrating cancer tissue, which led to the first theory linking cancer to the immune system. A few years later, Coley treated incurable tumors using a mixture of bacteria known as "Coley's toxin," which resulted in a significant decrease in tumor size despite an inconsistent clinical response. Burnet and Thomas proposed that the immune system can regulate the growth of cancer by identifying and eliminating tumor cells. Currently, most people acknowledge the immune system's involvement in preventing cancer spread. Specifically, the immune system and cancer cell interactions have been clarified by identifying the immunoediting process, which consists of three steps: elimination, equilibrium, and escape[1]. Tumor immunotherapy is often employed as a therapeutic approach for several malignancies. It eliminates malignancies by boosting or fortifying the body's defense system[2–6]. The most promising aspect of tumor immunotherapy is the use of immune checkpoint inhibitors, especially those targeting the PD-1/PD-L1 pathway[3,7].

Inhibitors of programmed cell death-ligand 1 (PD-L1) and programmed cell death receptor (PD-1) have demonstrated great preclinical and therapeutic promise for the treatment of cancer[8–10]. The binding of tumor-infiltrating lymphocytes to PD-1 on PD-L1, which is frequently found on the surface of tumor cells, inhibits T-cell function and induces tumor immune evasion[11–13]. Blocking PD-1/PD-L1 connections has emerged as a

[1]Institute of Molecular Biology and Biotechnology, The University of Lahore, Lahore, Pakistan. [2]Faculty of Medical and Health Sciences, The University of Adelaide, Adelaide, SA 5005, Australia. [3]Centre of Excellence in Molecular Biology, University of the Punjab, Lahore, Pakistan. [4]Department of Medical Laboratory, College of Applied Medical Sciences, Prince Sattam Bin Abdulaziz University, 11942 Al-Kharj, Saudi Arabia. [5]Department of Clinical Laboratory Sciences, College of Applied Medical Sciences, Jouf University, 72388 Sakaka, Aljouf, Saudi Arabia. ✉email: muhammad.umer4@mlt.uol.edu.pk

promising cancer treatment approach that boosts the immune response and activates T cells specific to tumors. In recent years, the FDA in the US has approved many antibody treatments that target PD-1 or PD-L1 for therapeutic use[14]. These drugs have shown notable advantages in a variety of solid tumor types, such as sustained clinical responses and manageable treatment-related toxicities[15,16]. Although these monoclonal antibodies have revolutionized cancer immunotherapy, they still have several drawbacks, including an incredibly long half-life, immunogenicity, restricted permeability, immuno-related adverse events (irAEs), challenging production processes, and high treatment costs[17].

Recent developments have produced small molecule inhibitors of the PD-1/PD-L1 pathway, some of which are currently undergoing clinical trials[3]. The Incyte Corporation is currently conducting phase II clinical trials for the most sophisticated inhibitor, INCB086550. Several other inhibitors are also undergoing phase I clinical trials[3]. Recent studies have examined the effects of dimerization on receptor internalization and degradation[18–22]. Unlike traditional inhibitors, the ligand HOU {2-[[3-[[5-(2-methyl-3-phenyl–phenyl)-1,3,4-oxadiazol-2-yl] amino] phenyl] methylamino] ethanol} is a multilingual inhibitor of PD-1/PD-L1 interaction that specifically targets the PD-1/PD-L1 axis. In malignant cells, the ligand HOU causes PD-L1 to dimerize, integrate, and be destroyed, while blocking PD-1/PD-L1 interactions. This causes PD-L1 to be taken up by the cytosol on the cell surface and initiates lysosome-dependent PD-L1 breakdown[18]. The PD-1/PD-L1 interactions were inhibited by HOU, with IC50 values of 24.5 nM. At a resolution of 2.4 Å, the structure of HOU linked to PD-L1 was identified (PDB entry 7DY7), proving that HOU stabilizes the PD-L1 dimer[18]. The unsubstituted phenyl ring of the biphenyl moiety was joined to A:Tyr56 via T-stacking. Biphenyl-linked amino-1,3,4-oxadiazole engages in π–π stacking with B:Tyr56, whereas the amino moiety forms a hydrogen bond with B:Gln66. The methoxy tail was joined to A:Asp122 by a hydrogen bond when facing the solvent. Because of its distinct structural and functional characteristics, HOU is a great starting point and a perfect template for finding structurally related compounds that may have improved pharmacokinetics and inhibitory efficacy. More work needs to be done before PD-1/PD-L1 axis inhibitors are approved for use in cancer treatment. Therefore, new potent small-molecule inhibitors targeting PD-1/PD-L1 are required. Our aim was to identify new analogs that would have superior drug-like qualities and preserve or increase the potency of HOU.

Given that in silico methodology is faster and less costly than trial-and-error procedures of experimental research, it can be highly beneficial in this respect[23]. Several studies have shown the value of using in silico techniques to study the mechanics of ligand–protein binding[24]. The use of in silico computational approaches has become a crucial drug discovery strategy, particularly with the emergence of PD-L1 inhibitors. The 3D crystal structure of human PD-L1 co-crystallized with small-molecule inhibitors has been used to determine the conformations of protein–ligand interactions and produce pharmacophore hypotheses using techniques such as molecular docking[25]. Scientists have used drug repurposing techniques that combine molecular docking, ligand-based virtual screening, and molecular dynamics simulations to identify FDA-approved drugs that may be PD-L1 inhibitors[26]. Molecular dynamics (MD) simulations were used to investigate the dynamics and mechanisms underlying the interactions between proteins and ligands. Specifically, several studies have demonstrated that a high degree of concordance between computational data and experimental results can be achieved by incorporating thermodynamic binding free energies and employing MD simulations of microsecond timescales in specified solvents[26,27]. These medications have demonstrated encouraging PD-L1 stability and binding affinity[28]. These techniques have facilitated the discovery of new PD-L1 inhibitors by allowing computational assessment of the binding energies of potential inhibitors[29].

Here, we described the identification of computational screening approach to screen databases of lead- and drug-like molecules that function as PD-1/PD-L1 cascade inhibitors and significantly boost immune cell capacity to combat cancer (Fig. 1).

Methodology

Target protein

PD-L1 (PDB ID: 7DY7)[30], is the target protein that may be studied in the Protein Data Bank (PDB) database (https://www.rcsb.org/). The PDB ID was chosen due to its better structural quality, as indicated by its X-ray crystallographic structure, a higher percentile and lower resolution (2.42 Å).

Protein preparation

The protein must be prepared before docking can begin because of defects in the protein's crystal structure from the Protein Data Bank, including incorrect bond ordering and missing side chains. The protein preparation wizard in the Maestro package of the Schrödinger software was then utilized to correct mislabeled components, assign correct bonds, fix bond order, add hydrogen, remove water molecules, detect disulfide bonds, and fill loops to proceed with the protein. Protein preparation identified any structural flaws in the protein and fixed them without altering their shapes[31].

Receptor grid generation

The three-dimensional receptor grid is where ligands can attach to PD-L1. A more precise estimation of the binding score for various ligand configurations is offered by the grid-based depiction of the receptor's shape and characteristics[32]. A receptor grid generation tool was used in the Maestro gliding program, and active site residues were specified to create the receptor grid for the protein. With regard to the x-, y-, and z-axes, the resolution of the receptor grid was positioned at 143.92, – 13.6, and 21.68, respectively[33]. Using Biovia Discovery Studio 2021, additional binding site investigations were carried out to ascertain the physicochemical properties relevant to the interaction with putative ligands.

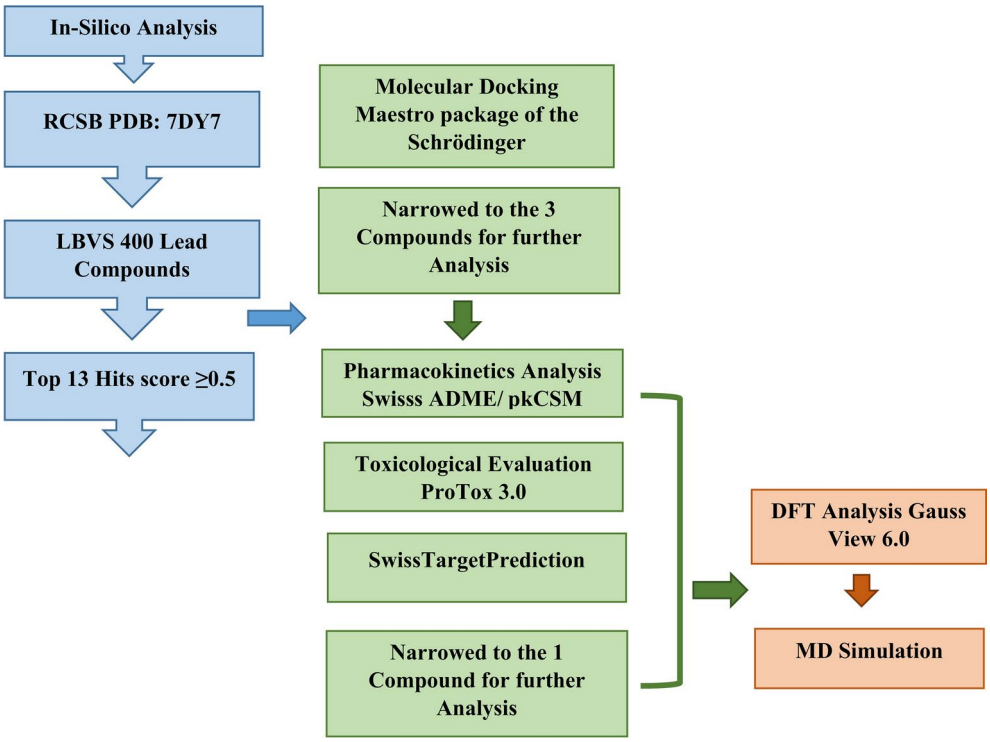

Fig. 1. Schematic Workflow of the current study by in-silico approach ((Created using Microsoft® PowerPoint® 2016 MSO (16.0.4266.1001) 64-bit).

Ligand based virtually screening

Virtual screening is a sophisticated computational technique that identifies tiny compounds for a specific target[34]. It mainly consists of ligand-based virtual screening[35,36]. Using SwissSimilarity (https://www.swisssimilarity.ch) as a template, the reference ligand 7DY7:HOU(CCL) was utilized in a similarity search[37]. In the process of ligand-based virtual screening, the ZINC20 lead-like compound library consisting of approximately 200,000 compounds[38] was evaluated using SwissSimilarity. This tool utilizes a hybrid 2D/3D screening approach that relies on FP2 and ES5D similarity metrics, which were initially developed for the SwissTarget Prediction tool[39]. Following the initial virtual screening, a total of 400 compounds were identified based on similarity to HOU. The combined similarity score represents the probability that two molecules share a common protein target. A cut-off score of ≥ 0.5 was applied, meaning only compounds with a 50% or higher likelihood of targeting the same protein as the reference ligand (HOU) were selected. This resulted in the identification of thirteen structurally similar compounds.

Ligand preparation

ChemDraw Professional 16.0 was used to manually design 2D structures of the chosen compounds. Chem3D 16.0[40], was then used to convert the 2D structures into 3D, and the files were saved as sdf. A library of the prepared 3D structures was created Using Biovia Discovery Studio 2021. The ligand preparation phase in Maestro 12.5, was then carried out by loading this library onto the LigPrep module. Next, geometry-optimized structures were obtained at pH 7.0 ± 2.0, using OPLS3, where the 3D structure of the ligand indicated its chirality[41].

Molecular docking

To complete the docking study using Maestro12.5, the Glide tool was used[42]. The interaction site of the target protein (7DY7) was docked with extreme precision (XP) using a ligand library, and ligand sampling was regarded as flexible sampling that did not require refining alone. Before the compound libraries were docked, the co-crystallized ligand was subjected to docking analysis to determine its binding affinity to the active site of the target protein. The interaction diagram of ligands with residues in the active site of the target protein was viewed using the ligand interaction tool. PyMOL Visualizer was used to display the three-dimensional structure of the hydrophobic interaction between ligands and binding site residues[43,44].

Structural interaction fingerprinting (SIFt) analysis

SIFt is a new technique for simulating and assessing three-dimensional protein–ligand interactions. The three-dimensional structural binding properties of the ligand–protein complex were transformed into a binary digit interaction fingerprint using the SIFt technique[45]. The SIFt panel in the Schrodinger suite 2020–3 was used to generate the interaction fingerprint of the docked complexes of the selected ligands. The receptor grid and compounds were selected as the input files. Hydrophobic, H-bond donor, and H-bond acceptor characteristics

were the types of interactions that, once created, contributed the most to the binding, according to the fingerprint finding. While appropriate colors indicate the type of contact between residues, numbers 1 and 0 indicate the presence or absence of interactions[46].

Pharmacokinetic parameters

SwissADME (http://www.swissadme.ch) was used to predict the ADME characteristics of the selected compounds and evaluate the synthetic accessibility of the newly developed compounds[47]. For computer-aided ADME research, the pkCSM webserver (http://biosig.unimelb.edu.au/pkcsm/prediction) was used to estimate the pharmacokinetic parameters[48]. These studies evaluated factors such as intestinal absorption level, CYP-binding metabolism, total clearance value, volume of distribution (VDss), and excretion associated with the prediction of AMES toxicity[49]. The oral bioavailability of the compounds was determined using ADMETlab (https://admetmesh.scbdd.com/)[50]. The Toxicological investigations were conducted using ProTox 3.0 (https://tox.charite.de/protox3/)[51]. LD50, liver toxicity, cytotoxicity, carcinogenicity, mutagenicity, immunotoxicity, adverse outcome (Tox21) pathways, and toxicity targets are among the quantifiable biological effects predicted using fragment propensities, molecular similarity, most frequent features, and machine learning techniques.

Screening of potential off-targets

Swiss Target Prediction (https://swisstargetprediction.ch/), (accessed on September 4, 2024), was employed for off-target prediction to identify potential unintended protein targets of the bioactive molecule[39]. The canonical SMILES string of the query compounds was input into the tool, which utilizes a ligand-based approach to predict likely protein interactions based on structural similarity to known bioactive molecules[52].

DFT studies (MEP/HOMO/LUMO analysis)

The B3LYP function was used for all calculations utilizing the Gaussian 06 package (Rev.E.01) with default parameters to execute density functional theory (DFT) computations[53], using the split valence polarization (SVP) basis set. Computing the electronic structures of atoms and molecules is possible by using this theory. The main objectives of the current investigation were to determine the frontier molecular orbital (FMO), molecular electrostatic potential (MEP), and ideal geometric characteristics. Guass View 6 was used to review the checks[54].

Molecular dynamics simulation

To investigate the stability of ligand binding, molecular dynamics (MD) simulations were performed on the corresponding ligand–protein complexes using the Desmond program. MD simulation was initiated using the top-binding conformation determined via Maestro docking. Using the OPLS_2005 force field, ligand interactions were modeled. The TIP3P water model was used to solve the ligand–protein combination and create a system for molecular dynamics simulations[43,55]. However, we utilized AMBER20 software (https://ambermd.org/GetAmber.php) to perform more thorough binding free energy calculations using the Molecular Mechanics/Poisson-Boltzmann surface area (MM-PBSA) technique[56]. To improve the verification of the results, we conducted all simulations using the AMBER program. To evaluate the inherent flexibility of PD-L1 in the unbound state, we also conducted a 100 ns MD simulation of the Apo PD-L1 protein using AMBER software[56,57].

Results

Analysis of binding site of prepared protein

First, the prepared structure of PD-L1 (PDB ID: 7DY7) (Fig. S1) was used to analyze the ligand-binding pocket of 7DY7. Initial investigations of the binding site were carried out utilizing the co-crystallized structure of PD-L1 (PDB ID: 7DY7) to partition it into multiple zones according to its intrinsic properties. The binding cavity of PD-L1 protein is shown in a series of color-coded maps (Fig. 2a–d) created using Biovia Discovery Studio 2021.

Each image emphasizes a different physicochemical characteristic that is important for the interaction with putative ligands. The aromatic map (Fig. 2a) highlights π-π interaction zones, primarily involving Tyr56 and Tyr123, which may stabilize aromatic ligands through stacking interactions. The hydrophobicity map (Fig. 2b) indicates that Met115, Tyr56 and Ala121 residues contribute to a hydrophobic pocket, favoring interactions with nonpolar ligand moieties. The hydrogen bond map (Fig. 2c) identifies Asp122, Met115, Ala121 and Tyr123 as key hydrogen bond acceptor, while Val76 acts as donor, supporting ligand anchoring through hydrogen bonds. Lastly, the solvent accessibility surface (SAS) map (Fig. 2d) suggests that the binding pocket is partially solvent-exposed, with residues like Gln66, Tyr56, Met115 and Ala121 influencing ligand solvation and binding dynamics.

Validation of docking protocol

The co-crystallized ligand CCL was used to re-dock into the protein-binding site to confirm the docking protocol[58]. As shown in Fig. 3, the docked crystallographic pose (yellow) and the projected structural pose (blue) exhibited strong alignment, confirming the accuracy of the docking procedure. The Schrödinger docking workflow produced a re-docking score of − 12.176kcal/mol, indicating high binding affinity and validating the methodology.

For docking, the receptor grid was defined with coordinates (x = 143.92, y = − 13.6, z = 21.68), ensuring precise placement of the ligand within the PD-L1 binding pocket. The XP (Extra Precision) scoring function was employed to enhance binding energy calculations and improve docking accuracy. Furthermore, all water molecules were removed before docking to prevent interference with ligand interactions and ensure a more reliable evaluation of receptor-ligand binding affinity. The successful re-docking of CCL demonstrated that the docking protocol could reliably reproduce experimental ligand-binding poses.

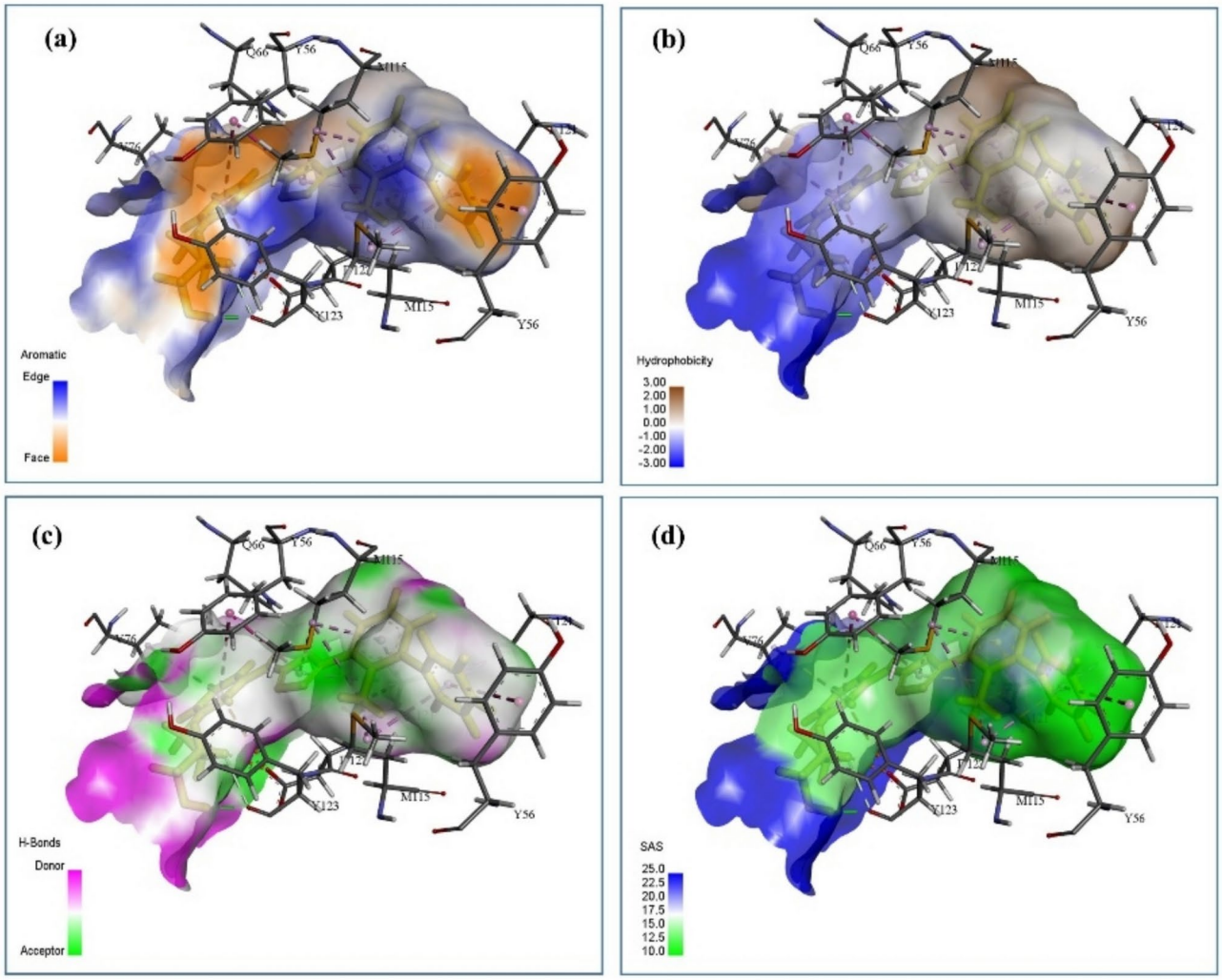

Fig. 2. A sequence of color-coded maps illustrating the binding cavity of the PD-L1 protein, each of which highlights a distinct physicochemical property relevant to the interaction with putative ligands, (**a**) aromatic map, (**b**) hydrophobicity map, (**c**) H-bonds map, (**d**) SAS (solvent accessibility surface) (Created with BIOVIA Discovery Studio Client 2021 version 21.1.0.20298).

Molecular docking analysis

We created 3D conformations for each virtual screening hit (Table S1) and docked them into the PD-L1 interacting site to evaluate the potential of the selected ligands to bind to the target. Schrödinger docking scores for all ligands ranged from −9.234 to −4.838 kcal·mol^{-1}, indicating favorable to moderate binding affinities. Table 1 shows the scores of all ligands chosen against PD-L1.

Four top-scoring ligands (−9.234 to −8.172 kcal/mol) that were accepted for comparison and analysis of the docked ligand binding pattern in PD-L1. Table 2 lists specific ligands with 2D and 3D structures as well as SMILES.

The ideal docking conformations for each ligand were saved and displayed graphically to investigate the differences in docking scores brought about by distinct interaction patterns. It is clear from all the ligand-binding sites analysis that the co-crystallized ligand CCL and selected ligands share same binding site in the PD-L1 protein (Fig. 4). Graphical analysis demonstrated that the hot residues in the ligand-binding site included Tyr123, Tyr56, Met115, Ala121, Asp122, Ser117, and Ile54 in the PD-L1-ligand complex-bound system (Fig. 4). Lig_1, Lig_10, Lig_11, and Lig_12 were surrounded by the common residues Tyr123, Tyr56, Met115, Ala121, Asp122, Ser117, and Ile54 (Fig. 5a). This is because all the selected top-scoring virtual screened ligands in PD-L1 complexes occupy the same cavity as that of 7DY7_CCL. On the other hand, Lig_1 and Lig_11 can bind with nearby 7DY7 residues to generate two and one hydrogen bond, respectively. Two hydrogen bonds were successfully formed by the Lig_1/PD-L1 bonded complex: the hydroxyl group of the ligand and the alpha-carboxyl group (–COOH) of Tyrosine Tyr123 in the donor motif, as well as the hydroxyl group of the ligand and the side-chain carboxyl group of the aspartic acid Asp122 of PD-L1 (Fig. 5a).

The –NH group in Lig_11 donated one hydrogen bond to the nearly positioned carboxyl group of Alanine Ala121, as illustrated in Fig. 5b. Salt bridges stabilized the docked complex Lig_11/PD-L1, connecting the

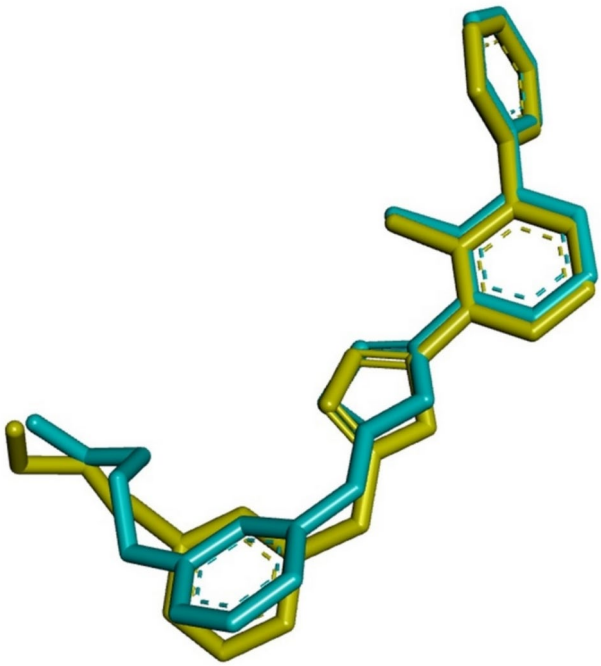

Fig. 3. Crystallographic or experiment pose (Yellow) of CCL and its predicted structure pose (Blue) (Created with BIOVIA Discovery Studio Client 2021 version 21.1.0.20298).

Code	Docking scores (kcal/mol)	Code	Docking scores (kcal/mol)
Lig_1	−8.512	Lig_8	−8.512
Lig_2	−7.758	Lig_9	−7.405
Lig_3	−7.538	Lig_10	−8.172
Lig_4	−6.105	Lig_11	−8.792
Lig_5	−4.838	Lig_12	−9.234
Lig_6	−7.541	Lig_13	−7.63
Lig_7	−6.962		
Standards	PD-L1_CCL		
	−12.176		

Table 1. Ligand docking scores against target 7DY7.

positively charged nitro group of the ligand to the negatively charged carboxylate group of aspartic acid Asp122 (Fig. 5b). However, in the cases of Mol_10 and Mol_12 (Fig. 5a), no hydrogen bonds were observed. Figure 5a illustrates how the presence of –OH and –NH in a certain structure makes them more polar, which leads to the formation of H-bonds. Furthermore, π–π stacking was observed to increase the stability of complexes by utilizing the benzene ring of the ligands (Lig_1, Lig_11, and Lig_12) with tyrosine Tyr56 (Fig. 5b). Compound Lig_10 (ZINC000426667711) did not show H-bonds or π-π stacking with the target residues, making it less favorable for further analysis.

Structural interaction fingerprinting (SIFt) analysis

Key residues involved in ligand binding are highlighted in Fig. 6, which depicts the hydrophobic, H-bond donor, and H-bond acceptor interactions between the selected ligands and the PD-L1 receptor. The reference co-crystallized ligand (CCL) contributed to its highest docking score of − 12.176kcal/mol by forming hydrophobic contacts with Tyr123, Tyr56, Met115, and Ala121 and an H-bond with Asp122 and Tyr123. Despite having a lower docking score of − 8.512kcal/mol, Lig_1 exhibited a similar pattern, forming a critical H-bond with Asp122 and maintaining a hydrophobic contact with Tyr56, Tyr123, Met115, and Ala121, indicating that it preserves the important binding properties of CCL.

Lig_12, on the other hand, had a marginally higher docking score than Lig_1 (− 9.234kcal/mol), but no H-bond interactions, suggesting that hydrophobic interactions rather than H-bond stabilization are the main forces behind its binding. Similarly, Lig_11 lacks a hydrophobic interaction with Tyr123, a crucial component shared by Lig_1 and CCL, although it forms a single H-bond with Ala121. Lig_10 had the lowest docking score

Code	Zinc ID	2D Structure	3D Structure	SMILES	Docking Score
Lig_12	ZINC000426513450	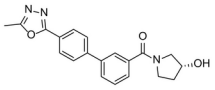	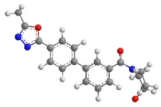	CC1=NN=C(C2=CC=C(C3=CC=CC(C(N4CC[C@H](C4)O)=O)=C3)C=C2)O1	–9.234
Lig_11	ZINC000195562471	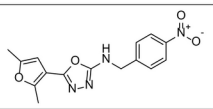	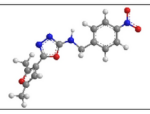	CC1=CC(C2=NN=C(O2)NCC3=CC=C([N+]([O-])=O)C=C3)=C(O1)C	–8.792
Lig_01	ZINC000000408954	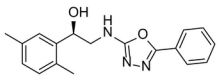	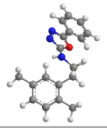	CC1=CC=C(C([C@H](CNC2=NN=C(C3=CC=CC=C3)O2)O)=C1)C	–8.512
Lig_10	ZINC000426667711	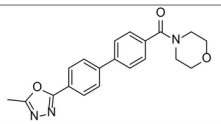	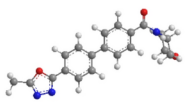	CC1=NN=C(C2=CC=C(C3=CC=C(C(N4CCOCC4)=O)C=C3)C=C2)O1	–8.172
CCL	N/A	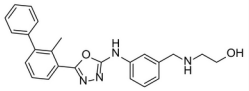	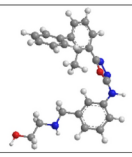	CC1=C(C2=CC=CC=C2)C=CC=C1C3=NN=C(NC4=CC=CC(CNCCO)=C4)O3	–12.176

Table 2. Structures (2D, 3D) and SMILES of the selected top scored ligands with respective docking score (kcal/mol).

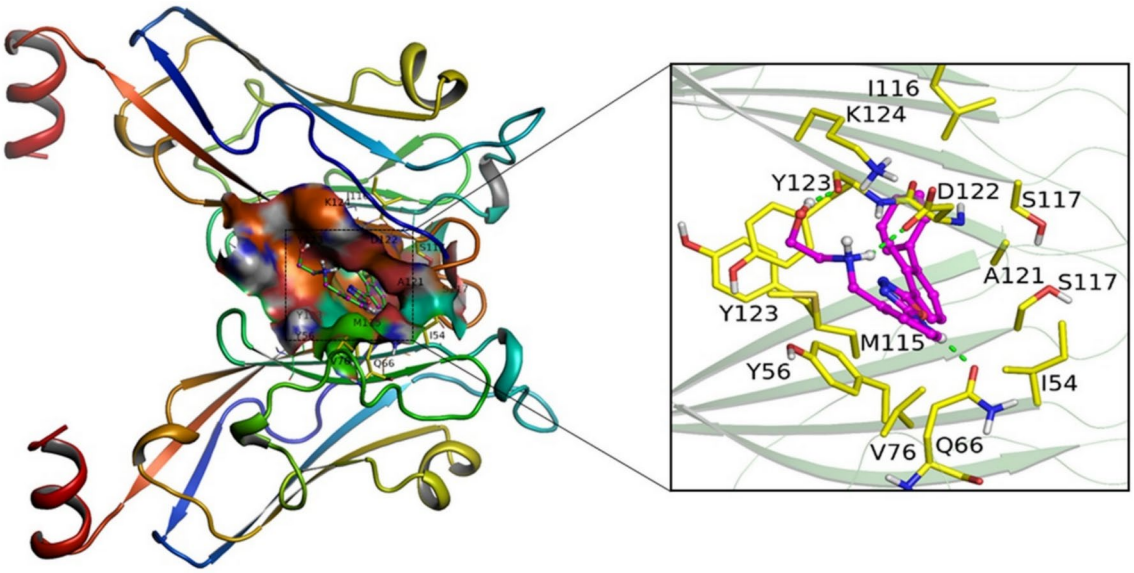

Fig. 4. Graphical analysis of Co-crystallized ligand (CCL) to binding site of PD-L1 (3D representation: PyMol Molecular Graphics system version 2.4.0).

(− 8.172kcal/mol) of these compounds, possibly because it does not have any H-bond contacts, even though it still maintains a hydrophobic connection with Tyr56 and Tyr123.

Since Lig_1 still has an H-bond with Asp122 and hydrophobic and aromatic interactions with residues Tyr56 and Tyr123—two essential characteristics that support robust receptor binding—it seems to be the most viable option overall in comparison to CCL. The results highlight the importance of striking a balance between hydrophobic and H-bonding contacts to increase ligand stability and affinity. To improve the binding efficacy of Lig_1 toward PD-L1, future alterations should concentrate on fortifying its interactions with crucial residues, such as Asp122, Tyr56, and Tyr123.

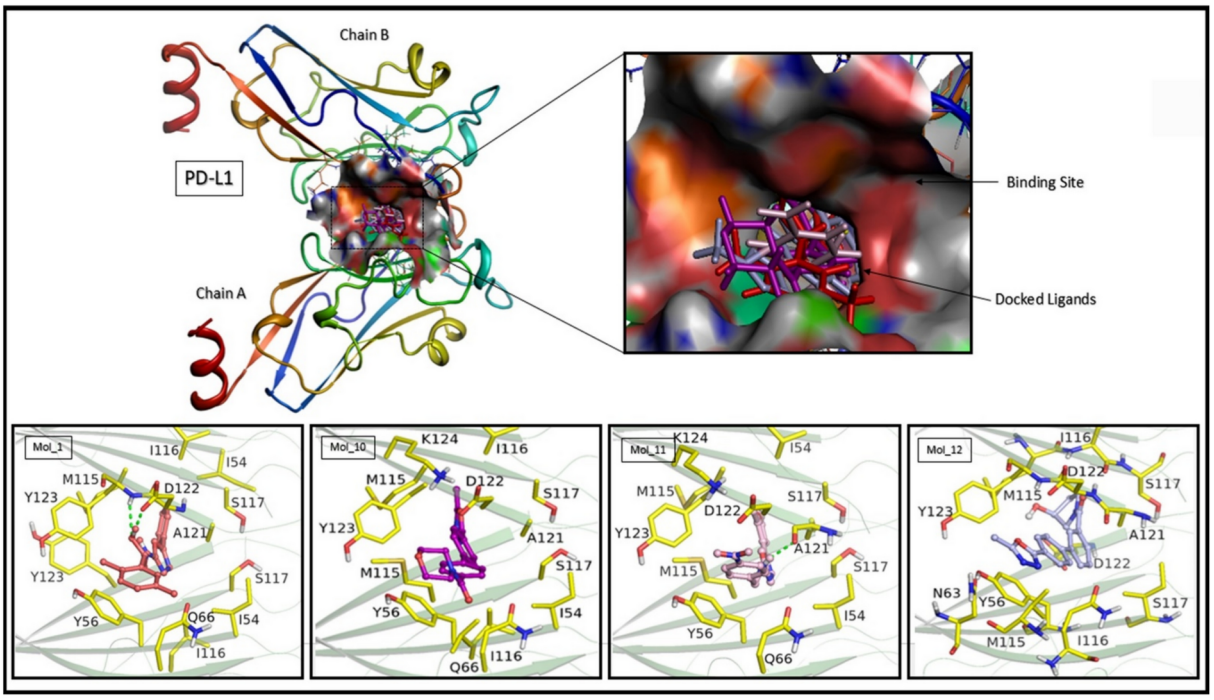

Fig. 5. (**a**) Graphical analysis of ligands (Lig_1, Lig_10, Lig_11 and Lig_12) to binding site of PD_L1 (3D representation: PyMol Molecular Graphics system version 2.4.0). (**b**) 2D interaction diagram of four selected compounds with residues of the target receptor: Lig_1, Lig_10, Lig_11, Lig_12 (2D representation: BIOVIA Discovery Studio Client 2021 version 21.1.0.20298).

Pharmacokinetic parameters

The compounds Lig_1, Lig_11, and Lig_12, which scored highest against other ligands, had a high likelihood of blocking the point of interaction of PD-1 to PD-L1, according to the results of molecular docking. The physicochemical and pharmacokinetic features of these top-scoring ligands were examined in more detail. The pharmacokinetic parameters of these ligands were computed using Swiss ADME and pKCSM, which also provided structural insights and predicted the adsorption, distribution, metabolism, excretion, and toxicity of these compounds.

Table 3 displays the results of the compound analysis, which indicated that all parameters examined for the chosen ligands were within the cutoff range of Lipinski's rule of five (ROF), and that no significant route of absorption resulted in a violation of the ROF. Additionally, the ADMETlab data in Fig. 7a display the colored zone of the pertinent physicochemical space for oral bioavailability, illustrating the ligands' competitiveness with the CCL.

The distribution of phytochemicals throughout several organs was subsequently evaluated using the blood–brain barrier's (BBB) permeability (Table 4). Figure 7b shows that Brain or Intestinal Estimated Permeation (BOILED-Egg), which displays small molecule polarity (TPSA) and lipophilicity (WLOGP), displays a similar outcome. The permeability of molecules up to the intestine or across the brain barrier was calculated using BOILED-Egg.

According to this study, the Pgp substrate, an inhibitor of the Pgp substrate, did not inhibit ligands of interest. Cytochrome P450 (CYP) is involved in drug metabolism. The most crucial cytochromes involved in metabolizing drugs are the CYP1, CYP2, and CYP3 families, which contribute to 80% of drug metabolism[59].

The ligands chosen from Table 4 inhibit the majority of CYP channels. Selected ligands, function as CYP2C19 inhibitors and CYP3A4 substrates, as the CCL positive control. Lig_1 was the selected ligand with the highest overall clearance rate, which was very close to that of CCL. Lig_1 and Lig_12 did not exhibit ADME toxicity (Table 4). Except for Lig_11, selected ligands and CCL were inhibitors of hERG II but non-inhibitors of hERG I (Table 4). Table 4 provides information on a wide range of other characteristics, including water solubility, Caco-2 permeability, skin permeability, fraction unbound (human), human intestinal absorption VDss (human), oral rat acute toxicity (LD_{50}), and skin sensitivity to ligands (Lig_1, Lig_11, Lig_12, and CCL).

Table 5 presents the toxicity of the top-scoring ligands as determined by ProTox 3.0, an online webserver that forecasts a compound's hazardous levels based on 33 models derived from in vitro and in vivo data[51]. The mutagenicity, hepatotoxicity, immunotoxicity, carcinogenicity and cytotoxicity are all examined in this study. Additionally, the server computes a lethal dose of 50% chemical exposure, which can result in test subject death, in order to determine the hazardous doses of compounds (LD_{50}). Lig_1 and Lig_11 were the least poisonous compounds chosen; they belonged to Class 4 as opposed to the other ligands that were chosen. These two ligands

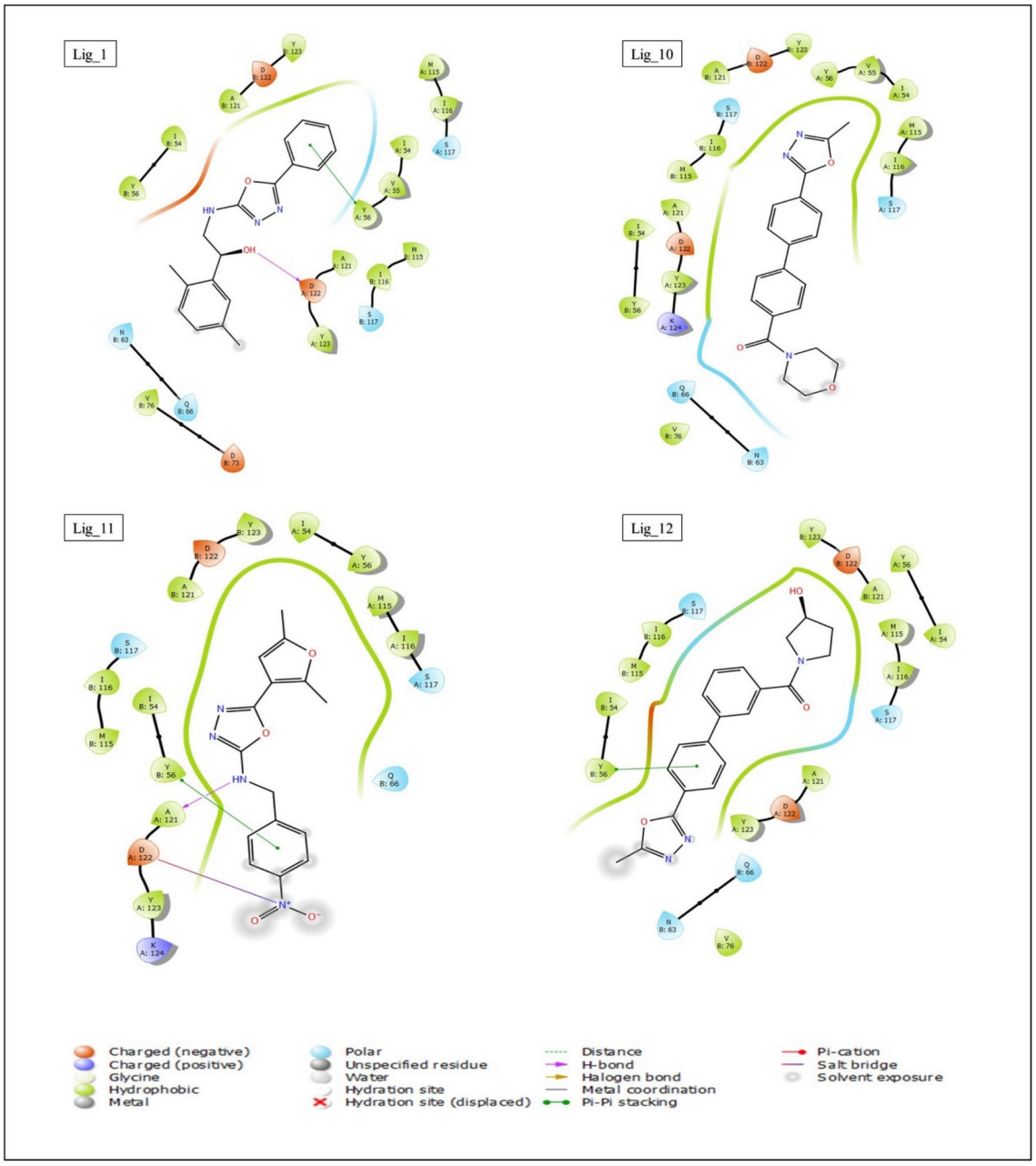

b

Fig. 5. (continued)

had the highest LD_{50} values of 800 and 550 mg/kg, respectively, implying that the compounds were harmful only at higher concentrations. If the substance is used in large doses, the immune system may become toxic[51].

Screening of potential off-targets

We examined the diversity and distribution of the anticipated target classes to assess the off-target impacts of the ligands. A lower probability of severe off-target interactions was suggested by Lig_1 (Fig. 8a), which displayed a more balanced distribution across several target classes without any predominant category. The off-target potential was stronger for Lig_11and Lig_12 (Fig. 8b,c), which showed a higher concentration of projected interactions in particular classes, especially Family A G protein-coupled receptors (46.7%). Although CCL (Fig. 8d) exhibited a wider distribution among different targets, it still had a dominant target class of 46.7%. Lig_1 is a more selective candidate than the others because it does not show dominance in any one off-target category, which suggests that it has a lower chance of unwanted interactions.

Title	A54	A56	A56	A115	A121	A121	A122	A122	A123	A123	A123	B54	B56	B56	B76	B115	B121	B123	B123
CCL	1	1	1	1	1	0	1	1	1	1	1	1	1	1	1	1	1	0	0
Lig_12	1	1	1	1	1	0	1	0	1	0	1	1	1	1	0	1	1	1	1
Lig_11	0	0	0	1	1	1	1	0	0	0	0	1	1	1	0	1	1	0	0
Lig_1	0	0	0	1	1	0	1	1	1	0	1	0	1	1	1	1	1	0	0
Lig_8	0	0	0	1	1	0	1	1	1	0	1	0	1	1	1	1	1	0	0
Lig_10	1	1	1	1	1	0	1	0	1	0	1	0	1	1	1	1	1	0	0
Lig_2	1	1	1	1	1	0	0	0	1	0	1	0	1	1	1	1	1	0	0
Lig_13	0	1	1	1	1	0	0	0	1	0	1	0	1	1	1	1	1	0	0
Lig_6	1	1	1	1	1	0	1	1	1	0	1	1	1	1	0	1	1	0	0
Lig_3	1	1	1	1	1	0	1	0	1	0	1	1	1	1	0	1	1	0	0
Lig_9	0	0	0	1	1	0	0	0	1	0	1	1	1	1	1	1	1	0	0
Lig_7	0	0	0	1	1	0	1	0	1	0	1	1	1	1	0	1	1	0	0
Lig_4	0	0	0	1	1	0	1	1	1	0	1	1	1	1	0	1	1	0	0
Lig_5	0	0	0	0	0	1	1	0	1	0	1	0	1	1	1	1	0	0	0

Fig. 6. Protein–ligand interaction fingerprinting for all selected ligands and residues taking part in the interaction site inside 4.0. Numbers 1 and 0 indicate whether the residues interact or not, respectively. The residues in orange, blue, green and grey indicate the hydrophobic, aromatic, H-bond acceptor and polar interactions, respectively (generated in Maestro v12.5).

Ligands	Lipophilicity index (≤ 5)	Molar mass (≤ 500 da)	Number of H-bond acceptors (≤ 10)	Number of H-bond donors (≤ 5)	Number of rotatable bonds	Violation of rules
Lig_1	3.49894	309.369	5	2	5	0
Lig_11	3.46674	314.301	7	1	5	0
Lig_12	2.91882	349.38	5	1	4	0
CCL	4.53752	400.482	6	3	8	0

Table 3. Screening of drug-likeness properties of selected compounds.

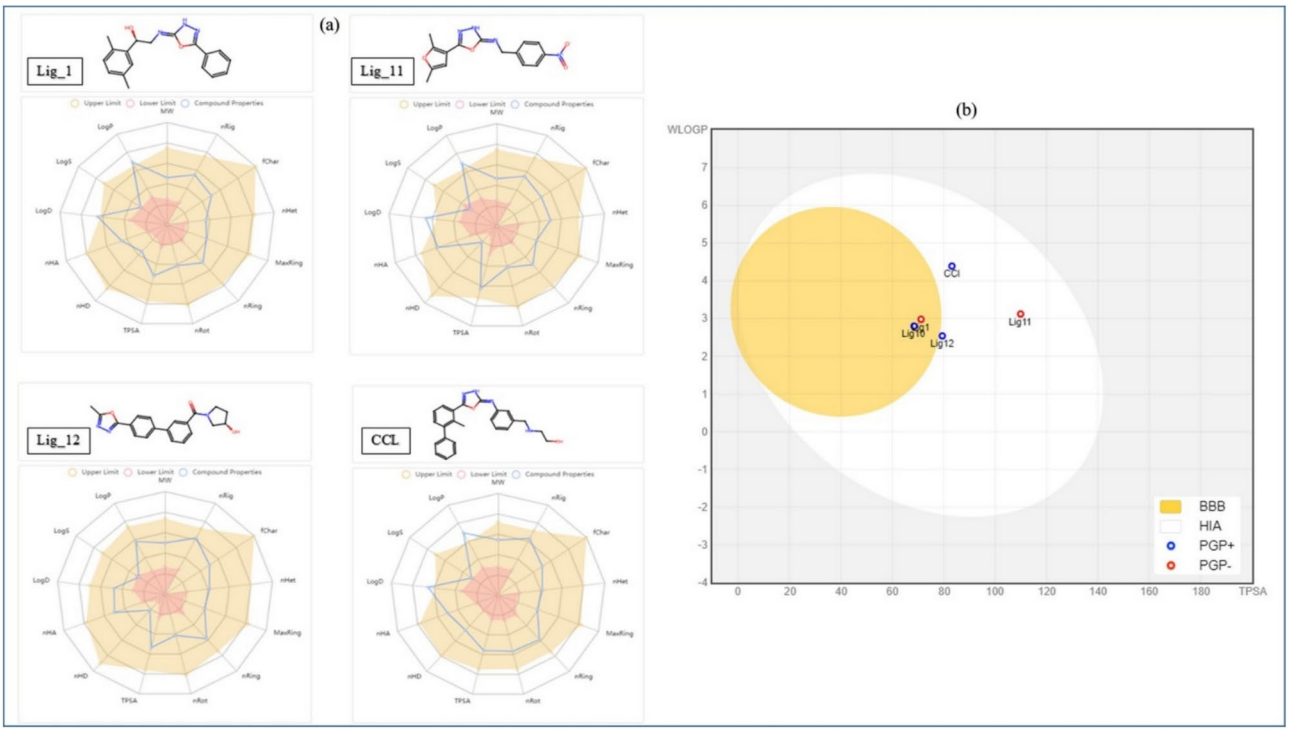

Fig. 7. (**a**) Bioavailability radar of selected compounds and CCL using the ADMElab tool (Assessed through ADMETlab) (**b**) BOILED-Egg results of three compounds in comparison with CCL (Assessed through SwissADME).

Pharmacokinetic properties		Selected ligands			
Properties	**Model name**	**Lig_12**	**Lig_11**	**Lig_1**	**CCL**
Absorption	Water solubility	− 4.272	− 4.859	− 4.339	− 5.235
	Caco-2 permeability	1.114	0.063	0.961	0.947
	Intestinal absorption (human)	94.519	94.658	91.663	91.556
	Skin Permeability	− 3.443	− 2.855	− 3.348	− 3.388
	P-glycoprotein substrate	Yes	Yes	Yes	Yes
	P-glycoprotein I inhibitor	Yes	Yes	Yes	Yes
	P-glycoprotein II inhibitor	Yes	No	No	Yes
Distribution	VDss (human)	− 0.66	− 0.77	0.37	0.625
	Fraction unbound (human)	0.143	0.143	0.372	0.302
	BBB permeability	− 0.367	− 0.74	− 0.205	− 0.426
	CNS permeability	− 2.127	− 2.199	− 2.313	− 2.404
Metabolism	CYP2C9 inhibitor	No	No	No	Yes
	CYP2D6 inhibitor	No	No	No	No
	CYP3A4 inhibitor	No	No	No	Yes
	CYP1A2 inhibitor	Yes	Yes	Yes	No
	CYP2C19 inhibitor	Yes	Yes	Yes	Yes
	CYP2D6 substrate	No	No	No	No
	CYP3A4 substrate	Yes	Yes	Yes	Yes
Excretion	Total Clearance	0.363	0.343	0.667	0.725
	Renal OCT2 substrate	No	No	No	No
Toxicity	hERG I inhibitor	No	No	No	No
	hERG II inhibitor	Yes	No	Yes	Yes
	AMES toxicity	No	Yes	No	No
	Max. tolerated dose (human)	0.705	0.955	0.479	− 0.087
	Oral Rat Acute Toxicity (LD_{50})	2.582	2.647	2.691	2.893
	Oral Rat Chronic Toxicity (LOAEL)	1.975	1.515	1.23	0.97
	Skin Sensitization	No	No	No	No
	Minnow toxicity	1.324	1.204	1.003	0.594
	T.Pyriformis toxicity	0.823	1.015	1.779	1.02

Table 4. pkCSM pharmacokinetic parameters of the selected Ligands.

DFT studies (MEP/HOMO/LUMO analysis)

Lig_1 (ZINC000000408954) with the most promising properties was selected for DFT analysis. We checked for Lig_1 (Fig. 9) using the Guass View 6. Frontier molecular orbitals (FMOs), HOMO, and LUMO are the three most significant orbitals in a molecule. The high EHOMO and low ELUMO values of a molecule result in its strong reactivity and low stability. Table 6 lists the EHOMO values of the studied ligands.

The DFT study of the selected ligand indicated that the dipole moment of Lig_1 was nearly twice that of CCL. Lig_1 also showed an ionization potential and electron affinity similar to that of CCL. The fact that the molecule is less likely to lose electrons indicates that it is more stable. The high electronegativity of Lig_1 denotes strong electron attraction, and the negative value of the electrochemical potential indicates the propensity of the compound to acquire electrons. Furthermore, the softness value of Lig_1 (0.236 eV) and hardness (2.11 eV) were extremely close to the conventional values of 0.241 eV and 2.069 eV respectively. Finally, the electrophilicity score of Lig_1 (2.603 eV) indicated that it is an electrophile (Table 6).

Molecular dynamics simulation

Desmond was mainly used for molecular dynamics (MD) simulations, which shed light on energy contributions, binding stability, and ligand–protein interactions. To ascertain the dynamic stability and intermolecular interactions as a function of 100 ns, classical molecular dynamics simulations were conducted using the selected Lig_1 (ZINC000000408954)/PD-L1 complex. The results were compared with the MD simulation paths of a reference docking complex and PD-L1/CCL inhibitor complex. The PD-L1/Lig_1 inhibitor complex's root mean square deviation (RMSD) values were first calculated from the corresponding docked posture as a function of the 100 ns simulation interval. These values were then compared with those of the PD-L1/CCL inhibitor complex (Fig. 10). The protein displayed notable changes (> 3.5 Å) when a particular docked complex of PD-L1/Lig_1 (blue) was simulated for 100 ns. Within 40 ns, the RMSD of the protein (4–6 Å) stabilized. A more dynamic and adaptable interaction with the PD-L1 binding pocket may be indicated by the higher RMSD of PD-L1/Lig_1. However, in the first 10 ns, PD-L1 and the HOU inhibitor (orange) showed significant variation (~ 4 Å), which was followed by a global minimum (~ 3 Å) until the simulation's conclusion.

Classification	Target	Lig_12		Lig_11		Lig_1		CCL	
		Pre	Pro	Pre	Pro	Pre	Pro	Pre	Pro
Organ toxicity	Hepatotoxicity	I	0.57	A	0.60	A	0.51	I	0.58
Toxicity end points	Carcinogenicity	A	0.55	A	0.84	A	0.61	A	0.63
	Immunotoxicity	I	0.99	I	0.98	I	0.99	A	0.54
	Mutagenicity	I	0.63	A	0.86	I	0.62	I	0.60
	Cytotoxicity	I	0.65	I	0.77	I	0.77	I	0.67
Tox21-nuclear receptor signalling pathways	AhR	I	0.81	I	0.64	I	0.70	I	0.77
	AR	I	0.96	I	0.97	I	0.93	I	0.91
	AR-LBD	I	0.96	I	0.99	I	0.99	I	0.98
	Aromatase	I	0.86	I	0.92	I	0.84	I	0.86
	ER	I	0.88	I	0.83	I	0.81	I	0.84
	ER-LBD	I	0.98	I	0.96	I	0.98	I	0.97
	PPAR-Gamma	I	0.93	I	0.96	I	0.92	I	0.92
	nrf2/ARE	I	0.97	I	0.91	I	0.94	I	0.95
Tox21-stress response pathways	HSE	I	0.97	I	0.91	I	0.94	I	0.95
	MMP	I	0.83	I	0.53	I	0.77	I	0.82
	p53	I	0.94	I	0.91	I	0.89	I	0.90
	ATAD5	I	0.95	I	0.91	I	0.90	I	0.91

Table 5. Toxicological parameters of the identified PD-L1 inhibitors according to Pro-Tox II. *Pre* prediction, *Pro* probability, *A* active; *I* inactive, *AhR* aryl hydrocarbon receptor, *AR-LBD* androgen receptor ligand binding domain, *ER-LBD* estrogen receptor ligand binding domain, *PPAR-Gamma* Peroxisome proliferator activated receptor gamma (PPAR-gamma), *nrf2/ARE* nuclear factor (erythroid-derived 2)-like 2/antioxidant responsive element (nrf2/ARE), *HSE* heat shock factor response element, *MMP* mitochondrial membrane potential, *p53* phosphoprotein (tumor supressor), *ATAD5* ATPase family AAA domain-containing protein 5.

Furthermore, PD-L1 and the CCL inhibitor had acceptable values for the estimated ligand root mean square fluctuation (RMSF) index (Fig. 11a), suggesting that the ligand docked to the protein was significantly stable. Lig_1 showing slightly higher fluctuations at specific regions, particularly around residues 115–130 and the C-terminal end. This suggests that Lig_1 induces localized flexibility in the PD-L1 binding pocket, which may contribute to dynamic binding interactions. However, the overall RMSF trends remain comparable, implying that both ligands maintain a relatively stable interaction with PD-L1.

The overall similarity in Rg values indicates that both ligands maintain the structural integrity of the protein, though CCL allows for slightly greater expansion over the simulation time. PD-L1/Lig_1 (blue) had consistent Rg values for 100 ns ranging from 20.0 to 21.5 Å, indicating the least amount of Cα atomistic motion of the constant residues. Compactness was used to assess the stability of protein folding throughout the simulation. For PD-L1/CCL (orange), the Rg values ranged from 21.0 to 22.5 Å (Fig. 11b). The RMSD and RMSF results were corroborated by later stable Rg values, which indicated compactness in protein folding.

To investigate the sub-conformational structural alterations in reteplase, we examined the Gibbs free energy landscape (FEL), which illustrates the way in which a protein's free energy interacts with the molecule's three-dimensional structure in opposition to PC1 and PC2. The 2D and 3D images of the FEL analysis for Lig_1 are shown in Fig. 12a, together with ΔG values ranging from 0 to 7 kJ moL^{-1}. Blue is used to identify the minimum global energy conformation. The dimensions and form of the smallest energy area reveal the stability of the building. The increased stability of the associated structures is suggested by more concentrated blue spots throughout the MD simulation, as the thermodynamically most stable structure is at a minimum on the free energy (ΔG) surface (Fig. 12a–b). In PCA plots, Lig_1 exhibits a broader distribution across PC1 and PC2, indicating more conformational variability, which aligns with its fluctuating RMSD. The free energy landscape (FEL) for Lig_1 shows a deeper, well-defined global minimum, suggesting that despite its higher RMSD, it still reaches energetically favorable conformations. Conversely, CCL has a more restricted PCA spread and fragmented energy basins, correlating with its relatively stable RMSD behavior (Fig. 12b).

The dynamic cross-correlation matrix (DCCM) was used to quantify correlations between the dynamic motions of the four inter-domains of the reteplase to obtain additional insight into conformational changes (Fig. 13). To visualize the level of correlation between the nobilities, a color-coded scheme was developed; the blue color indicates a low correlation with the residues, whereas the red to pale green hues show highly connected mobility. In 7DY7/Lig_1, stronger correlations (dark blue regions) are observed, particularly in residues 1–100 and 150–200, indicating extensive cooperative motions in these regions (Fig. 13a). This suggests that Lig_1 induces greater conformational flexibility, potentially allowing the protein to adopt multiple structural states.

Conversely, in 7DY7/CCL, the correlations appear less pronounced and more dispersed, with fewer strongly correlated regions. This indicates a more rigid protein conformation, implying that CCL may stabilize the protein more effectively, reducing large-scale fluctuations (Fig. 13b).

To further validate these findings, we re-run simulations of CCL and Lig_1 using AMBER, employing the MM-PBSA method for binding free energy calculations. Additionally, an Apo PD-L1 simulation (100 ns) was

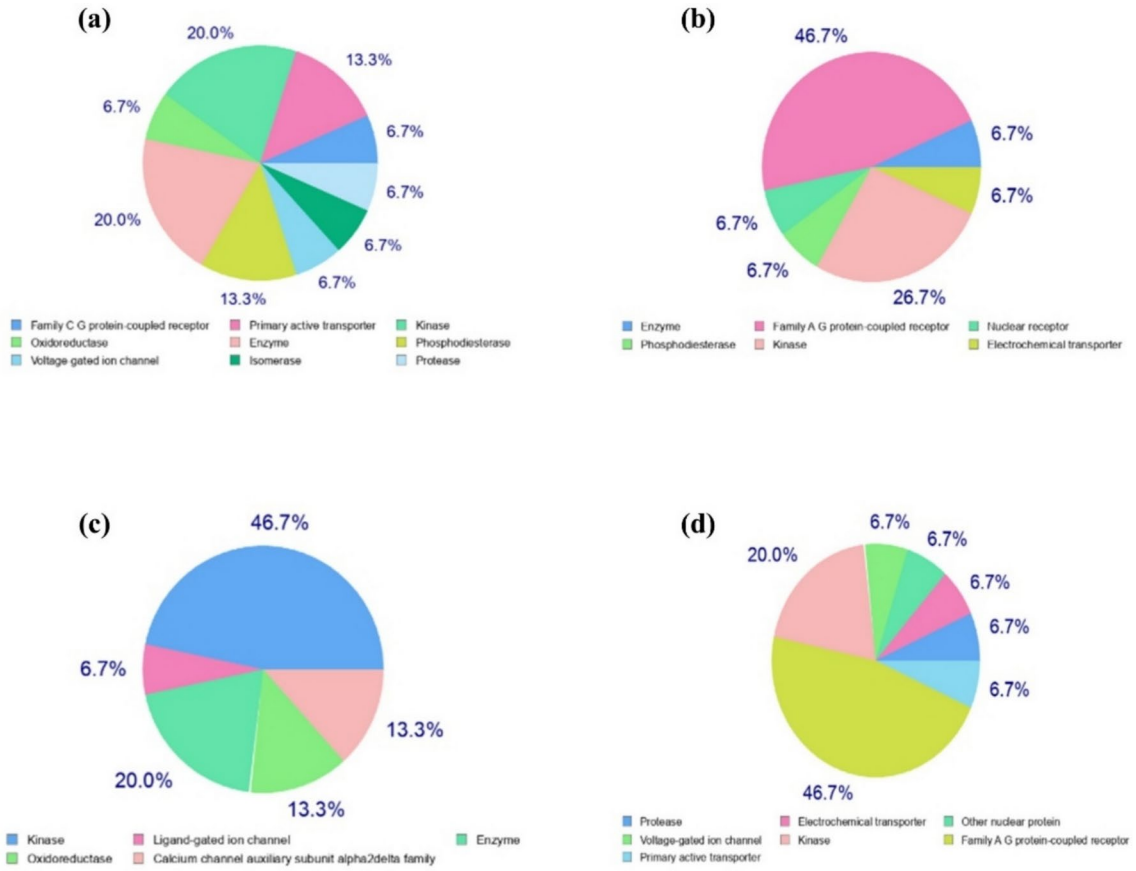

Fig. 8. Swiss Target Prediction of the Top-Hit Compounds (**a**) Lig_1, (**b**) Lig_11, (**c**) Lig_12 and (**d**) CCL (Assessed through SwissTargetPrediction).

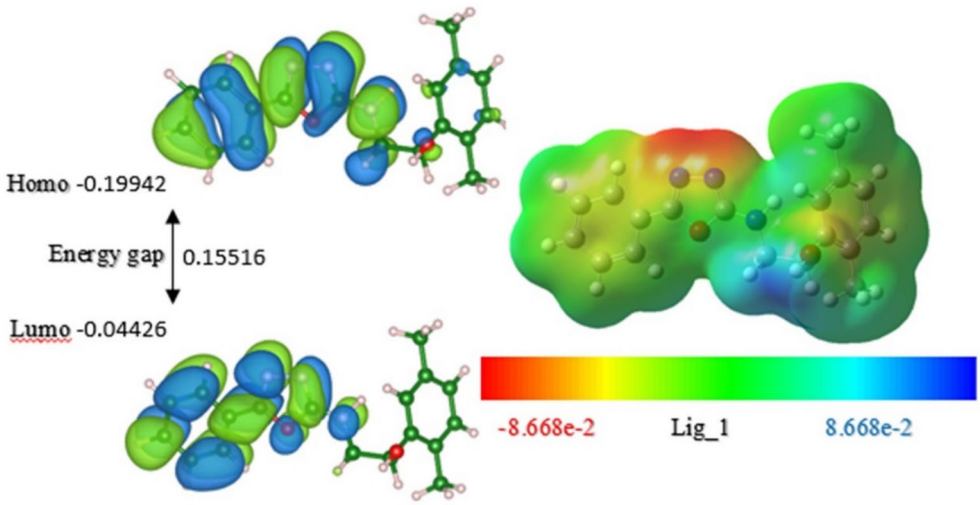

Fig. 9. The optimized structure, HOMO and LUMO of Lig_1 (FMOs and MEP visualized on VESTA Version 3 and Gauss view software 6.0 respectively).

performed using AMBER to assess the intrinsic flexibility of the unbound protein. Based on RMSD, the structures were grouped in the AMBER simulation. Multidimensional scaling was then applied to the central structures of each cluster to identify common conformations of the PD-L1 structure across various binding states (Fig. S2). The comparative results between Desmond and AMBER, detailed in the Supplementary Information, confirm

Parameters for DFT analysis	Ligands	Standard
	Lig_1	CCL
Dipole moment (Debye)	7.059	3.558
HOMO (a.u.)	−0.199	−0.208
LUMO (a.u.)	−0.044	−0.056
Energy Gap (ΔE_{Gap}) (a.u.)	0.155	0.152
Ionization Potential (eV)	5.426	5.671
Electron affinity (eV)	1.204	1.532
Electronegativity χ (eV)	3.315	3.601
Electrochemical potential μ (eV)	−3.315	−3.601
Hardness η (eV)	2.111	2.069
Softness S (eV)	0.236	0.241
Electrophilicity ω (eV)	2.603	3.133

Table 6. DFT analysis parameters of the selected ligand with standard CCL.

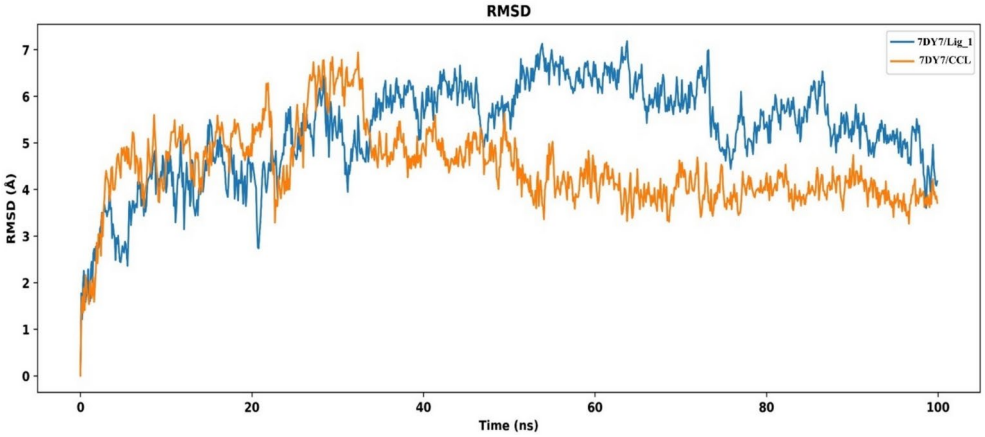

Fig. 10. RMSD plots for the PD-L1-Ligands; from each docked complex's individual 100 ns MD simulation trajectory, the ligand RMSD values were calculated as the protein-fit ligand. Protein RMSD values were retrieved for the alpha carbon atoms (Generated using Desmond module of Maestro v12.5).

the reliability of our primary simulations and highlight the robustness of CCL and Lig_1 as potential candidates (Figs. S2–S5).

The AMBER simulation results confirm the consistency of the molecular dynamics behavior and are in good agreement with Desmond's findings. Similar to Desmond, the CCL complex in AMBER exhibited consistent RMSD values, indicating strong binding and a few variations inside the pocket. In contrast, Lig_1 displayed higher RMSD fluctuations, indicating greater structural flexibility. This is also seen in the Desmond data, where Lig_1 deviates more than the CCL. Furthermore, the Apo protein is comparatively stable, with RMSD values consistently lower than those of the ligand-bound complexes. This confirmed that ligand binding, especially to PD-L1, introduces significant structural dynamics (Fig. S2). The overall flexibility seen in the PCA projections may be attributed to the changes in critical regions, especially loop structures, as highlighted by the RMSF results (Fig. S3). The diffuse pattern in the correlation matrix indicated that the Apo protein had relatively weak cross-correlations across residues. Given its inherent flexibility and dynamic character in the absence of ligand binding, this implied a lack of coordinated motion (Fig. S4). Furthermore, the structural plasticity of the apoprotein is reinforced by the wider conformational space displayed in its free energy landscape (Fig. S5).

Calculations of binding free energy (BFE) according to MMGB/PBSA and per residue-free energy decomposition analysis

The binding free energies (BFE) of each complex were computed to assess its structural and energetic properties. The binding free energy was determined after 1000 samples were collected in the last 2 ns of the simulations. The BFE was determined using a molecular mechanics-based analysis that included molecular mechanics MMGB/PBSA modules integrated into AMBER20 software. According to the MM/PBSA analysis, CCL has a favorable binding energy because of greater electrostatic (ΔE_ele = − 19.86 kcal/mol) and van der Waals (ΔE_vdw = − 63.22 kcal/mol) interactions. To partially counteract these advantageous interactions, CCL also has a greater solvation penalty, especially in polar solvation energy (ΔG_ele,sol (PB) = 28.72 kcal/mol, ΔG_ele,sol (GB) = 26.97 kcal/mol) (Fig. 14a). In contrast, Lig_1 maintains strong interactions (ΔE_vdw = − 42.79 kcal/mol,

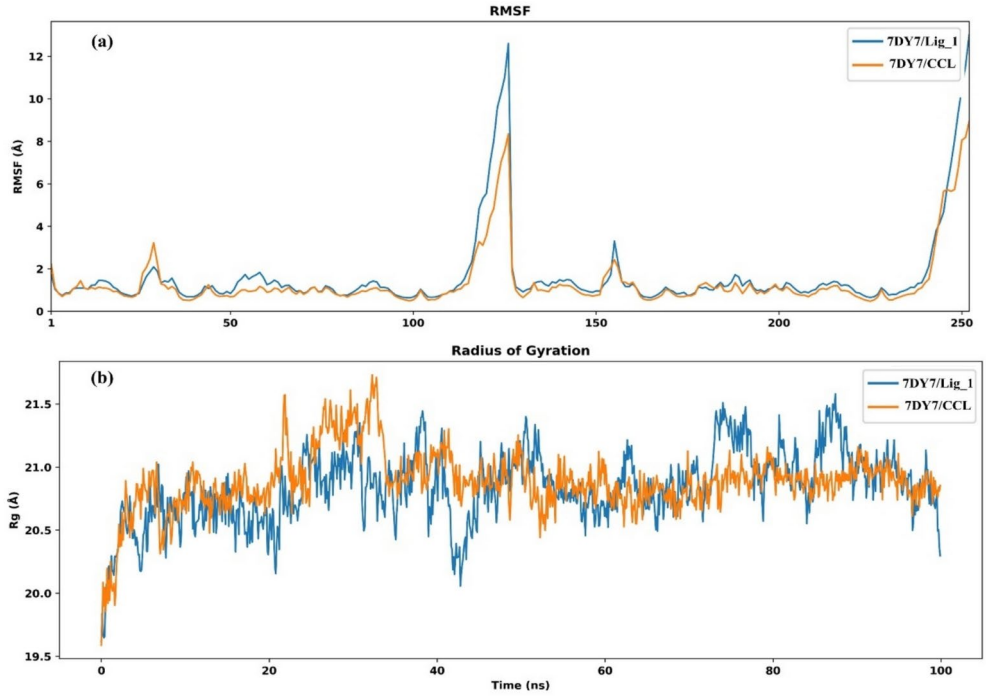

Fig. 11. The RMSF values for each residue in the protein structure of the two protein–ligand complexes, which were subjected to MD simulations for 100 ns, were compared in (**a**), while the radius of gyration of the protein over time was analyzed in (**b**) (Generated using Desmond module of Maestro v12.5).

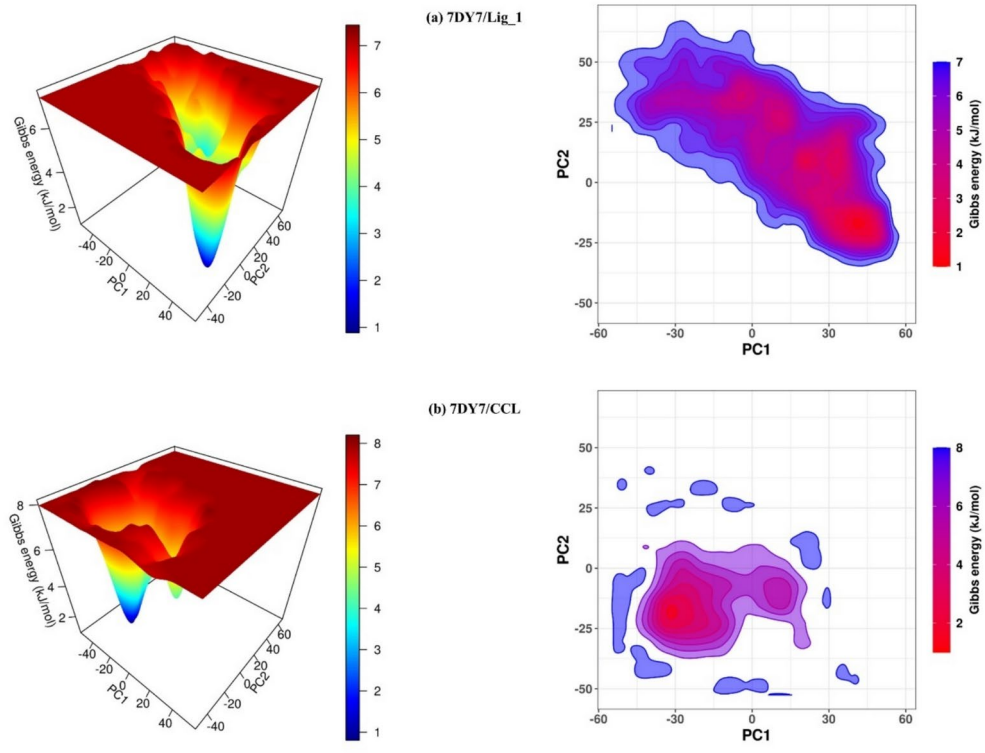

Fig. 12. (**a**–**b**) Two main eigenvectors of Lig _1's (**a**) and CCL (**b**) Gibbs free energy landscape (FEL). Lower-energy conformations are shown by the blue region, meta-stable states are shown by the yellow region, and high-energy conformations are shown by the red region (Generated using Desmond module of Maestro v12.5).

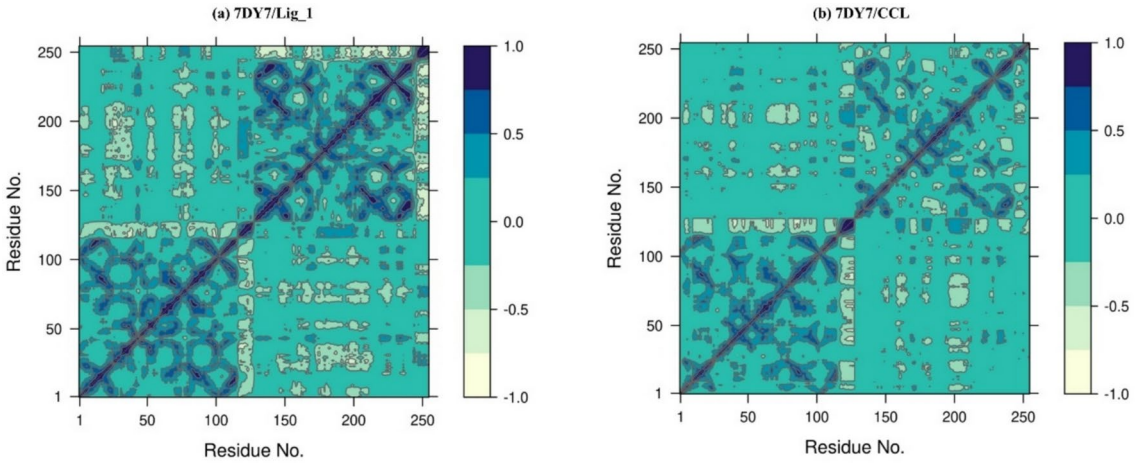

Fig. 13. Cross-correlation matrix showing coordinate fluctuations for Cα atoms around the mean positions during MD simulation: positive correlations are represented by blue, whereas negative correlations are represented by off-white. (**a**) 7DY7/Lig_1 (**b**) 7DY7/CCL (Generated using Desmond module of Maestro v12.5).

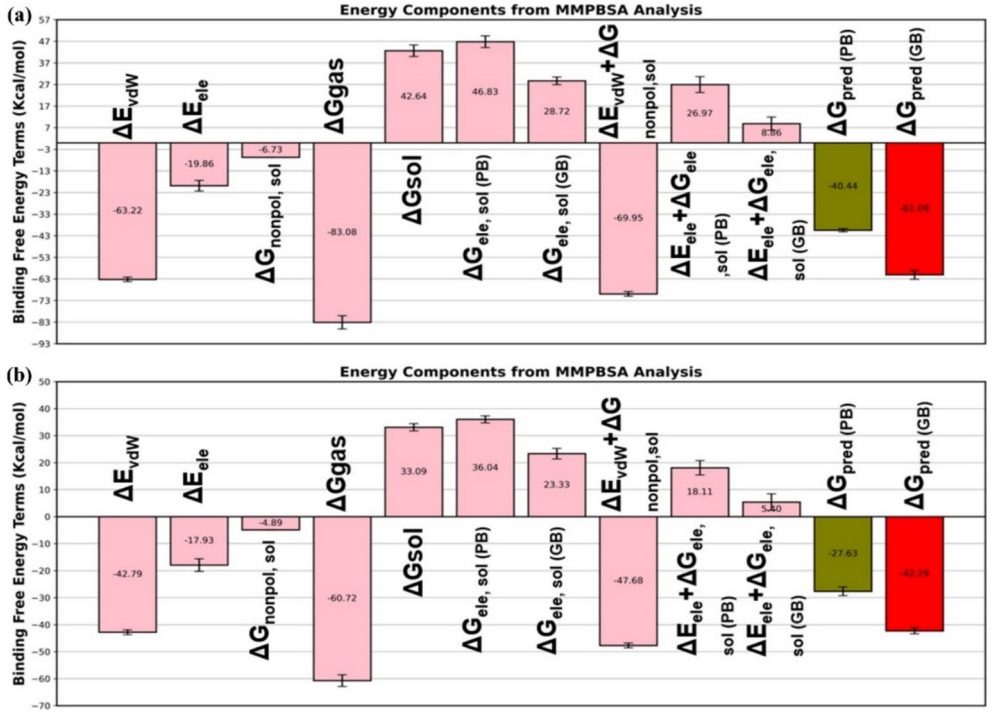

Fig. 14. Comparison for the binding free energy terms applied for PD-L1, CCL (**a**), Lig_1 (**b**) (Generated using AMBER 20).

ΔE_ele = − 17.93 kcal/mol) while having a smaller solvation penalty (ΔG_ele,sol (PB) = 23.33 kcal/mol, ΔG_ele,sol (GB) = 18.11 kcal/mol) (Fig. 14b). Based on its better-balanced binding energy profile and potential for additional optimization as a contender, Lig_1 may be a viable substitute for CCL.

Using the MMGB/PBSA method script in Amber, the calculated binding free energy was broken down into specific residue contributions, providing a deeper understanding of the binding mechanism and intricate interactions that stabilize CCL and Lig_1 in PD-L1. Using quantitative breakdown data makes it much easier to understand how different chemicals connect with one another. The most important residues affecting the binding free energy of the complexes are shown in Fig. 15a,b. The majority of interactions originate from the binding site residues, including Tyr39 (56), Met98 (115), Ala104 (121), Asp105 (122), Tyr106 (123), Ile163 (54A), Tyr165 (56A), Gln175 (66), Val185 (76), Met224 (115), and Ala230 (121), which play crucial roles in

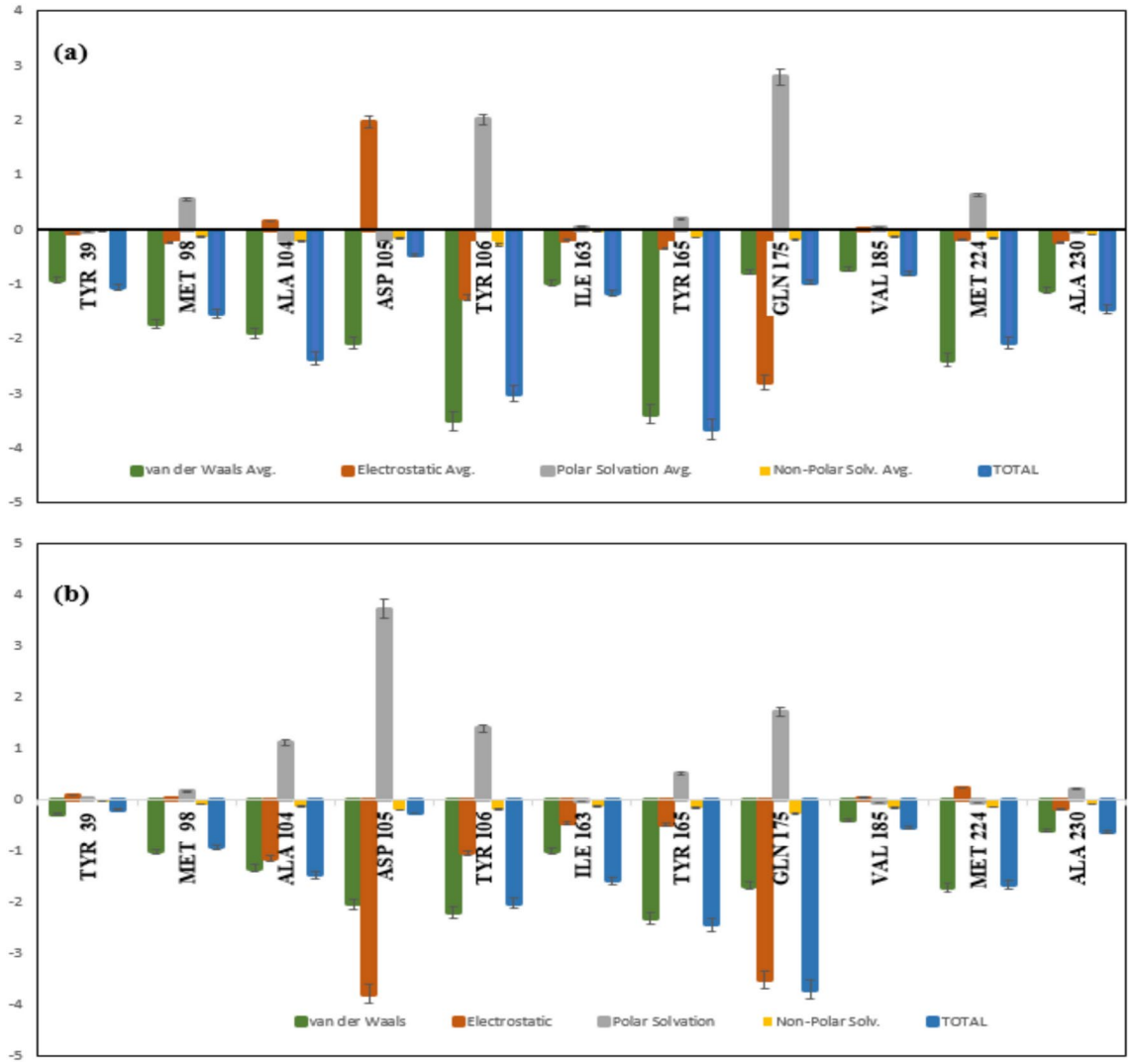

Fig. 15. Per residue energy decomposition analysis of CCL (**a**) and Lig_1 (**b**) (Generated using AMBER 20).

contributing to negative energy. In contrast, certain residues are closely bound to each other and have a more significant impact on the formation of the receptor-ligand complex.

The contributions of various energy components across important residues were shown by the binding free energy breakdown of the CCL (Fig. 15a) (Table S2). Significant polar solvation penalties (gray bars) are present in Tyr106 and Gln175, which typically disrupt binding. Their overall binding energies (blue bars) are still favorable, although, indicating that the solvation penalty is offset by stabilizing contributions from van der Waals interactions (green) and electrostatic interactions (orange). However, strong van der Waals interactions allow Asp105 to maintain its stabilizing function despite this electrostatic penalty (green bar), whereas hydrophobic residues such as Ile163 and Val185 mostly gain from van der Waals interactions. The complex interplay between the advantageous and unfavorable forces in determining the total binding strength was highlighted by this analysis.

The energy decomposition for Lig_1 showed variations in the residue contributions compared to the CCL (Fig. 15b) (Table S3). Similar to CCL (the reference molecule), Tyr106 and Gln175 showed notable polar solvation penalties (gray bars), but their overall binding energies (blue bars) were still favorable because of the compensatory effects of electrostatic (orange) and van der Waals (green) interactions. Asp105 demonstrated a substantial stabilizing effect because of its extremely advantageous electrostatic interactions. However, this contribution was partially offset by a significant positive polar solvation energy, indicating an energetic penalty associated with desolvation, whereas Ile163, Tyr165, and Val185 maintained stabilizing van der Waals interactions. Certain residues (such as Ala104 and Met224) have marginally different interaction patterns than CCL, which may indicate differences in ligand-binding modes and overall stability.

This suggests that while Asp105's contribution as electrostatic and polar solvation is unfavorable, other interaction types help offset this penalty, leading to an overall stabilizing effect in the binding pocket.

Discussion

Compared to other immunotherapeutic approaches, immune checkpoint blockage has been authorized in this case as clinically relevant and remarkably successful[60,61]. Novel anticancer medicines may target the PD-1/PD-L-1 pathway[62]. Currently available PD-L1-targeting drugs aim to block protein–protein interactions (PPI) in general, as well as functionally suppress the interaction between tumor-intrinsic PD-L1 and PD-1[63]. Wang et al. found that compound (HOU) facilitates the dimerization, internalization, and breakdown of PD-L1 while also preventing interactions between PD-1 and PD-L1[18].

Here, using Wang's compound HOU as a model, we described the identification and refinement of new compounds that were taken from the ZINC drug-like library[64] of SwissSimilarity[37] to suppress the PD-1/PD-L1 pathway, which might significantly stimulate immune cell antitumor immunity.

In the current in silico investigation, certain compounds (with a cut point ≥ 0.5 during the similarity search) were evaluated against the PD_L1 receptor using Maestro 12.5, PyMol Visualizer, and further analyzed through ADMET and DFT analysis. Thirteen compounds almost identical to the reference medications were identified. We were able to predict ligand-PD_L1 interactions at the molecular level using a potent in silico structure-based technique known as molecular docking. The target protein 7DY7 was obtained from the Protein Data Bank (PDB)[18]. All the chosen compounds made contact in the same way as the HOU/PD_L1 complex (7DY7), according to the docking data of ligands/PD_L1. Table 1 shows that the computed binding scores of the chosen ligands, Lig_12, Lig_11, Lig_1, and Lig_10, for this targeted region were − 9.234, − 8.792, − 8.512, and − 8.172 kcal/mol, respectively. Based on the chosen docked structures, nearly all of the inhibitors were shown to have both hydrophobic and hydrogen contacts with the residue(s), with the majority of these interactions being hydrophobic (Fig. 5b). According to the available experimental data, the results demonstrated that the chosen compounds bound to important residues in the protein model. The common residues in the ligand-binding region are Tyr123, Tyr56, Met115, Ala121, Asp122, Ser117, and I54[18]. PD-1 and PD-L1 exhibit polar and hydrophobic interactions within a wide, flat interaction region (1870 Å2). The small ligands binding site is positioned at the center of the PD-1 interacting surface. Tyr56, Met115, and Tyr123 are displaced to form a cylindrical hydrophobic cavity that holds the biphenyl groups of small molecules[1]. Each of the ligands chosen had this type of interaction with the target (Fig. 5a,b). Most of the hydroxyl group interactions between the ligands and residues occurred in the donor moiety. As previously disclosed, tyrosine residue Tyr56 is expected to be involved in π–π stacking in the 2.42 Å, PD_L1 crystal structure in conjunction with HOU. Analysis of the interacting site of the generated protein revealed that the aromaticity at residue tyrosine Tyr56 in chains A and B was mainly directed toward the face, indicating a significant aromatic interaction potential in this region (Fig. 5a,b).This connection is believed to be crucial for selective suppression and to promote PD-L1 dimerization, internalization, and degradation[18]. With the exception of Lig_10, our selected ligands, Lig_1, Lig_11, and Lig_12, also interacted with Tyr56, as shown in Fig. 5a, suggesting that they were potent PD_L1 inhibitors. A T-stacking interaction formed between the phenyl ring in Lig_1 and A:Tyr56. Additionally, the hydroxyl group next to the chiral center strengthened the hydrogen bonds, particularly with Asp122. The binding mode of Lig_1 in the docking investigations showed a more favorable orientation with π–π stacking at Tyr56 at 3.84 Å, increasing its total interaction strength in comparison to Lig_11 and Lig_12. Wang et al. claimed that HOU interacts with dimers via its crystal structure after penetrating the deep hydrophobic pocket of the PD-L1 dimer interface. The unsubstituted phenyl ring of the biphenyl moiety interacts with A:Tyr56 via T-stacking. While the biphenyl-linked amino-1,3,4-oxadiazole stacked with B:Tyr56 in a π–π pattern, the amino moiety formed a hydrogen bond with B:Gln66. The methoxy tail was attached to A:Asp122 via a hydrogen bond with its back to the solvent[18].

In silico drug-likeness prediction, in conjunction with additional toxicology analysis, was performed to better understand the selected compounds. The physiochemical parameters of the identified compounds were estimated using the Swiss ADME and pKCSM. The compounds' analysis revealed that, for the chosen ligands, all examined parameters fell within the cutoff range of Lipinski's rule of five (ROF) and that there was no violation of the ROF with a significant route of absorption, as indicated in Table 3.

Subsequently, the permeability of the blood–brain barrier (BBB) was used to assess the dispersion of phytochemicals across different organs. The polarity (TPSA) and lipophilicity (WLOGP) of small compounds are shown in Fig. 7. The permeability of molecules via the brain barrier or up to the intestines is estimated using the BOILED-Egg[65]. The data indicate that Lig_1 was near yellow (egg yolk), whereas CCL, Lig_12, and Lig_11 fell into the white zone. Certain molecules in the cooked egg have a blue circle with a red center (PGP+), indicating that they are P-glycoprotein (P-gp) substrates that may be actively effluxed out of cells, including brain cells. This may lessen their efficacy in treating brain tumors, and some of the chemicals are indicated by a red circle (PGP-), indicating a substance that is good for maintaining greater concentrations in brain cells since it is not a P-glycoprotein substrate. Since Lig_1 is situated in the yellow region, it is more likely to pass through the blood–brain barrier (BBB) and sustain higher concentrations in the brain than P-gp substrate. This makes it a better candidate for the treatment of brain tumors. The white zone is where compounds Mol_12 and CCL were found, indicating poor BBB penetration. PGP + (Blue Circle with White Center, P-gp substrate), which might further limit its availability in the brain. Ligand Lig_11 is positioned far outside the yellow region, indicating that its capacity to cross the BBB may be restricted; nonetheless, the absence of P-gp interaction is advantageous[30]. Ligand Lig_1 (in the yellow region and PGP-), followed by Lig_11 (near the yellow region and PGP-), are the best candidates for treating brain tumors. Furthermore, cytochrome P450 (CYP) plays a major role in the drug's metabolism. The CYP1, CYP2, and CYP3 families of cytochromes are most important in drug metabolism, accounting for 80% of drug metabolism[48]. Suppression of CYP1A2 and CYP2C19 by the compound gives rise to a moderate possibility of drug-drug interactions. It is advantageous that there is no inhibition of CYP2D6, CYP2C9, or CYP3A4, because this lowers the possibility of important drug-drug interactions through these enzymes. However, inhibition of CYP1A2 and CYP2C19 should be carefully considered, especially if patients

are taking other medications metabolized by these enzymes (Table 4)[47]. In addition, the toxicity of the selected ligands were illustrated in Table 5 using ProTox 3.0, an online webserver that forecasts a compound's harmful concentrations based on 33 models derived from in vitro and in vivo data[51]. Mol_1 and Mol_11 were the least hazardous compounds chosen; they belonged to Class 4 as opposed to the other ligands that were chosen. These two ligands had the highest LD_{50} values—800 and 550 mg/kg, respectively—implying that the compounds were only harmful at greater concentrations. If the substance is used in larger doses, the immune system may become toxic[51].

Toxicity testing, ADMET analysis, and bioactivity predictions indicated that Lig_1 was the top choice for DFT investigation. Functional molecular orbitals (FMOs) include details on electron transport, stability, and chemical reactivity, in addition to describing the interactions of a molecule with other molecules[66,67]. FMO orbitals are crucial in the study of medicine because they help identify a distinct and efficient way in which medication molecules interact with neighboring biomolecules. Therefore, it is crucial to analyze FMO electron cloud plots to derive accurate qualitative data regarding the vulnerability of the drug to interacting with biological species[68]. Because adding electrons to a high-lying LUMO and/or removing electrons from a low-lying HOMO is energetically favorable for any potential reaction, a large HOMO–LUMO gap is associated with high kinetic stability and low chemical reactivity, whereas a small HOMO–LUMO gap is significant for low chemical stability[69]. For CCL and Lig_1, the HOMO energies of the compounds in water were −0.208 and −0.199 a.u., respectively. The LUMO values of the complexes were −0.056 and −0.044 a.u., which translate into band gaps of 0.152 and 0.155 a.u., respectively. Both interacting chemicals have a small energy gap, which suggests that they are more sensitive and conducive. Global reactivity descriptors (GRD) were calculated to gain a comprehensive understanding of the chemical stability and reactivity of the selected ligand toward the target receptor (Table 6). Calculations were performed for the ionization energy, electron affinity, chemical potential, hardness, softness, and electronegativity. The stability and chemical reactivity of a molecule determine its ionization energy (I). It was determined how much energy was needed to extract a single electron from a molecule[70]. For the target receptor (PD-L1), Lig_1 is the most reactive ligand. Its 5.426 eV ionization energy was comparable to that of the CCL (5.671 eV). Electron affinity (A) is the energy generated when an electron is introduced to a neutral molecule. Rapid electron absorption is more likely to occur when there are strong electron affinities[71]. Because of its similar electron affinity to CCL, Lig_1 is a promising candidate for CCL in terms of its electrical properties and potential binding interactions. The ability of a molecule to withstand electron cloud deformation 70 is measured by its chemical hardness[70]. The bandgap energy of a soft molecule is modest, whereas that of a hard molecule is large. Compared with stiff molecules, soft molecules polarize more readily[70]. The compound showed balanced resistance to changes in electron density and moderate reactivity, with a hardness (η) value of 2.111 eV. The molecule is stable, but it still has sufficient reactivity to interact with its target, according to the matching softness (S) value of 0.236 eV. The ability of a molecule to draw electrons is measured by its electronegativity (χ)[70]. As shown in Table 6, Lig_1 (2.603 eV) and CCL (3.133 eV) had the highest electronegativity. The stability of the chosen ligand Lig_1 (ZINC000000408954) toward the target as a whole may promote advantageous binding interactions.

MD simulations were performed to further assess the binding pattern and interaction analysis of the selected ligand, Lig_1 (ZINC000000408954) (Figs. 10, 11, 12, 13, 14 and 15). Researchers can use this computational approach to analyze the flexibility and stability of binding interactions, providing valuable information on structural changes that may compromise the efficacy[72]. To determine the sampling pattern and dynamic stability, the root-mean-square deviations (RMSD) of the protein, CCL, and specific ligands were computed. In contrast to CCL, Lig_1 changed the shape of the protein from 4 to 6 Å, indicating that a conformational shift may occur if a ligand binds to a flexible region of the protein[73]. According to earlier research on PD-L1 inhibitors, some ligands cause conformational changes in the binding site, which increases RMSD values while preserving strong interactions[74,75]. The results of our 100 ns MD simulation are in good agreement with earlier research carried out over longer simulation timelines (150 and 200 ns), showing that small-molecule inhibitors can cause structural changes in PD-L1, resulting in higher RMSD values. In longer simulations, inhibitors, such as BMS-200 and BMS-202, caused conformational flexibility in the binding pocket and promoted PD-L1 dimerization, exhibiting similar patterns[74,75]. The RMSF distribution across residues confirms the dynamic stability of the systems under investigation and offers data in support of the RMSD conclusions. Also, the RMSF found that both ligands (Lig_1 and CCL) had the same sequence for binding to PD-L1. These variations are in line with earlier research that showed that inhibitors enhance the flexibility of important residues while maintaining the overall stability of the protein–ligand complex by causing the majority of residues to remain rigid. Their possible involvement in dynamic interactions with ligands is suggested by higher fluctuations in the loop areas[76]. Further supporting the idea that our 100 ns simulation is adequate to capture important dynamic changes that lead to PD-L1 inhibition are the observed residue-level fluctuations. Hence, Lig_1 might be a good option because it might provide more flexibility and dynamic interactions that could improve its function or binding in ways that are different from ligand 2's (CCL). Furthermore RMSF values was increasing upon ligand binding (compared to the apo form) (Fig. S3), this suggests that the binding of CCL or Lig_1 is inducing flexibility rather than stabilizing the protein. The protein may undergo structural rearrangements to accommodate the ligand, leading to higher fluctuations[57].

Additionally, the interaction of Lig_1 with PD-L1 goes beyond binding affinity; it also aids in PD-L1 dimerization, internalization, and degradation, all of which are critical in interfering with immune evasion pathways. The hydrophobic pocket at the PD-L1 dimer interface is occupied by Lig_1, which reinforces π–π stacking with A:Tyr56 and stabilizes contact with B:Tyr56 through its oxadiazole moiety, similar to compound HOU (PDB: 7DY7), which promotes PD-L1 dimerization. The PD-L1 dimer is further stabilized by the hydrogen bond facilitated by Asp122 by the hydroxy-substituted chiral site in Lig_1. One important distinction from straightforward PD-1/PD-L1 inhibition is the internalization and lysosomal destruction of monomeric PD-L1, which results from this instability. Lig_1 maintains immune activation and inhibits the PD-1/PD-

L1 relationship by actively decreasing PD-L1 expression, which may improve antitumor immunity beyond competitive protection.

However Lig_1 ((ZINC000000408954) should undergo lead optimization and experimental investigations, to confirm binding affinity, cell-based PD-L1 degradation assays and functional studies to evaluate immune activation. Such experimental validation would help determine whether Lig_1 effectively promotes PD-L1 degradation and disrupts PD-1/PD-L1 signaling, paving the way for its potential development as a therapeutic PD-L1 inhibitor.

Conclusion

To determine whether ligand-based screening drugs are good candidates for inhibiting the PD-L1 protein, a rational therapeutic strategy for managing the PD-1/PD-L1 axis block was developed. Computational techniques were used in conjunction with substantial drug-likeness and docking energy. The hit candidate Lig_1 (ZINC000000408954) was identified; it did not violate Lipinski's ROF and showed some excellent pharmacokinetic features owing to its unique molecular interactions and binding affinities with PD-L1. While the compound Lig_1 is close to ideal, this study suggests that to improve its drug-likeness and overall bioavailability, it may be necessary to address or improve that particular characteristic. The potential of the hit candidate Lig_1 (ZINC000000408954) as a new PD-1/PD-L1 inhibitor should be thoroughly elucidated by in vitro and in vivo experiments.

Data availability statement

The dataset analyzed during the current study are available in the manuscript and its supplementary files. *Data Transparency*: Rest assured, I have ensured that all data, materials, software applications, and custom code supporting the claims made in this article are in full compliance with field standards. It is important to note that I have taken into account the possibility of individual journal policies regarding research data sharing, considering the norms and expectations of our discipline.

Received: 27 December 2024; Accepted: 5 May 2025
Published online: 30 September 2025

References

1. Fantacuzzi, M., Paciotti, R. & Agamennone, M. A comprehensive computational insight into the PD-L1 binding to PD-1 and small molecules. *Pharmaceuticals (Basel, Switzerland)* https://doi.org/10.3390/ph17030316 (2024).
2. Xu-Monette, Z. Y., Zhou, J. & Young, K. H. PD-1 expression and clinical PD-1 blockade in B-cell lymphomas. *Blood* **131**, 68–83. https://doi.org/10.1182/blood-2017-07-740993 (2018).
3. Cai, S. et al. Design, synthesis, and evaluation of PD-1/PD-L1 small-molecule inhibitors bearing a rigid Indane scaffold. *Eur. J. Med. Chem.* **256**, 115468 (2023).
4. Awan, S. J. et al. Guar gum in therapeutics: A succinct exploration. *Bull. Biol. Allied Sci. Res.* **2024**, 60. https://doi.org/10.54112/bbasr.v2024i1.60 (2024).
5. Malik, A., Islam, J., Zaib, G., Saadia, H. & Zahid, A. Correlation of oxidative stress markers in multiple biofluids of end-stage renal disease patients. *Bull. Biol. Allied Sci. Res.* **2024**, 86. https://doi.org/10.54112/bbasr.v2024i1.86 (2024).
6. Malik, A. et al. Role of oxidative stress and immune response alterations in asthmatic pregnant females. *Bull. Biol. Allied Sci. Res.* **2024**, 85. https://doi.org/10.54112/bbasr.v2024i1.85 (2024).
7. Lin, X., Lu, X., Luo, G. & Xiang, H. Progress in PD-1/PD-L1 pathway inhibitors: From biomacromolecules to small molecules. *Eur. J. Med. Chem.* **186**, 111876. https://doi.org/10.1016/j.ejmech.2019.111876 (2020).
8. Algazi, A. P. et al. Clinical outcomes in metastatic uveal melanoma treated with PD-1 and PD-L1 antibodies. *Cancer* **122**, 3344–3353 (2016).
9. Reck, M. et al. Pembrolizumab versus chemotherapy for PD-L1–positive non–small-cell lung cancer. *N. Engl. J. Med.* **375**, 1823–1833 (2016).
10. Swami, U., Monga, V., Bossler, A. D., Zakharia, Y. & Milhem, M. Durable clinical benefit in patients with advanced cutaneous melanoma after discontinuation of anti-PD-1 therapies due to immune-related adverse events. *J. Oncol.* **2019**, 1856594 (2019).
11. Zou, W., Wolchok, J. D. & Chen, L. PD-L1 (B7–H1) and PD-1 pathway blockade for cancer therapy: Mechanisms, response biomarkers, and combinations. *Sci. Transl. Med.* **8**, 328rv324. https://doi.org/10.1126/scitranslmed.aad7118 (2016).
12. Boussiotis, V. A. Molecular and biochemical aspects of the PD-1 checkpoint pathway. *N. Engl. J. Med.* **375**, 1767–1778. https://doi.org/10.1056/NEJMra1514296 (2016).
13. Boxberg, M. et al. PD-L1 and PD-1 and characterization of tumor-infiltrating lymphocytes in high grade sarcomas of soft tissue–prognostic implications and rationale for immunotherapy. *Oncoimmunology* **7**, e1389366 (2018).
14. Xin Yu, J. et al. Trends in clinical development for PD-1/PD-L1 inhibitors. *Nat. Rev. Drug Discov.* **19**, 163–164. https://doi.org/10.1038/d41573-019-00182-w (2020).
15. Dirix, L. Y. et al. Avelumab, an anti-PD-L1 antibody, in patients with locally advanced or metastatic breast cancer: A phase 1b JAVELIN solid tumor study. *Breast Cancer Res. Treat.* **167**, 671–686. https://doi.org/10.1007/s10549-017-4537-5 (2018).
16. Zhang, H. et al. Discovery of novel small-molecule inhibitors of PD-1/PD-L1 interaction via structural simplification strategy. *Molecules* https://doi.org/10.3390/molecules26113347 (2021).
17. Tang, J., Shalabi, A. & Hubbard-Lucey, V. M. Comprehensive analysis of the clinical immuno-oncology landscape. *Ann. Oncol.: Off. J. Eur. Soc. Med. Oncol.* **29**, 84–91. https://doi.org/10.1093/annonc/mdx755 (2018).
18. Wang, T. et al. Discovery of small-molecule inhibitors of the PD-1/PD-L1 axis that promote PD-L1 internalization and degradation. *J. Med. Chem.* **65**, 3879–3893 (2022).
19. Park, J. J. et al. Checkpoint inhibition through small molecule-induced internalization of programmed death-ligand 1. *Nat. Commun.* **12**, 1222. https://doi.org/10.1038/s41467-021-21410-1 (2021).
20. Koblish, H. K. et al. Characterization of INCB086550: A potent and novel small-molecule PD-L1 inhibitor. *Cancer Discov.* **12**, 1482–1499. https://doi.org/10.1158/2159-8290.Cd-21-1156 (2022).
21. Sheema, et al. Molecular identification of HCV genotypes among injecting drug users having HCV and HIV co-infection. *Bull. Biol. Allied Sci. Res.* **2024**, 71. https://doi.org/10.54112/bbasr.v2024i1.71 (2024).
22. Ullah, A. et al. An overview of hepatitis c virus and liver cirrhosis in Pakistan. *Bull. Biol. Allied Sci. Res.* **2024**, 64. https://doi.org/10.54112/bbasr.v2024i1.64 (2024).

23. Singh, R., Bhardwaj, V. K. & Purohit, R. Inhibition of nonstructural protein 15 of SARS-CoV-2 by golden spice: A computational insight. *Cell Biochem. Funct.* **40**, 926–934 (2022).
24. Singh, R. & Purohit, R. Computational analysis of protein-ligand interaction by targeting a cell cycle restrainer. *Comput. Methods Programs Biomed.* **231**, 107367 (2023).
25. Chandrasekaran, J. et al. Computational design of PD-L1 small molecule inhibitors for cancer therapy. *Mol. Divers.* **27**, 1633–1644 (2023).
26. Bhardwaj, V. K. & Purohit, R. A comparative study on inclusion complex formation between formononetin and β-cyclodextrin derivatives through multiscale classical and umbrella sampling simulations. *Carbohyd. Polym.* **310**, 120729 (2023).
27. Bhardwaj, V., Singh, R., Singh, P., Purohit, R. & Kumar, S. Elimination of bitter-off taste of stevioside through structure modification and computational interventions. *J. Theor. Biol.* **486**, 110094 (2020).
28. Sobral, P. S., Luz, V. C., Almeida, J. M., Videira, P. A. & Pereira, F. Computational approaches drive developments in immune-oncology therapies for PD-1/PD-L1 immune checkpoint inhibitors. *Int. J. Mol. Sci.* **24**, 5908 (2023).
29. Wang, Y. et al. PD-1-targeted discovery of peptide inhibitors by virtual screening, molecular dynamics simulation, and surface plasmon resonance. *Molecules* **24**, 3784 (2019).
30. Bronner, S. M. et al. Design of a brain-penetrant CDK4/6 inhibitor for glioblastoma. *Bioorgan. Med. Chem. Lett.* **29**, 2294–2301 (2019).
31. Rolta, R. et al. In silico screening of hundred phytocompounds of ten medicinal plants as potential inhibitors of nucleocapsid phosphoprotein of COVID-19: An approach to prevent virus assembly. *J. Biomol. Struct. Dyn.* **39**, 7017–7034. https://doi.org/10.1080/07391102.2020.1804457 (2021).
32. Sakhawat, A. et al. In silico and in vitro analyses to investigate the effects of vitamin C on VEGF protein. *J. Taibah Univ. Med. Sci.* **19**, 775–789. https://doi.org/10.1016/j.jtumed.2024.06.008 (2024).
33. Sahayarayan, J. J. et al. In-silico protein-ligand docking studies against the estrogen protein of breast cancer using pharmacophore based virtual screening approaches. *Saudi J. Biol. Sci.* **28**, 400–407. https://doi.org/10.1016/j.sjbs.2020.10.023 (2021).
34. Rester, U. From virtuality to reality: Virtual screening in lead discovery and lead optimization—a medicinal chemistry perspective. *Curr. Opin. Drug Discov. Devel.* **11**, 559–568 (2008).
35. Elseginy, S. A. & Anwar, M. M. Pharmacophore-based virtual screening and molecular dynamics simulation for identification of a novel DNA gyrase B inhibitor with benzoxazine acetamide scaffold. *ACS Omega* **7**, 1150–1164. https://doi.org/10.1021/acsomega.1c05732 (2022).
36. Elseginy, S. A. Virtual screening and structure-based 3D pharmacophore approach to identify small-molecule inhibitors of SARS-CoV-2 M(pro). *J. Biomol. Struct. Dyn.* **40**, 13658–13674. https://doi.org/10.1080/07391102.2021.1993341 (2022).
37. Zoete, V., Daina, A., Bovigny, C. & Michielin, O. SwissSimilarity: A web tool for low to ultra high throughput ligand-based virtual screening. *J. Chem. Inf. Model* **56**, 1399–1404. https://doi.org/10.1021/acs.jcim.6b00174 (2016).
38. Irwin, J. J. et al. ZINC20: A free ultralarge-scale chemical database for ligand discovery. *J. Chem. Inf. Model.* **60**, 6065–6073 (2020).
39. Daina, A., Michielin, O. & Zoete, V. SwissTargetPrediction: Updated data and new features for efficient prediction of protein targets of small molecules. *Nucleic Acids Res.* **47**, W357–W364 (2019).
40. O'Boyle, N. M. et al. Open babel: An open chemical toolbox. *J. Cheminform.* **3**, 33. https://doi.org/10.1186/1758-2946-3-33 (2011).
41. Onikanni, S. A. et al. Computational and preclinical prediction of the antimicrobial properties of an agent isolated from *Monodora myristica*: A novel DNA gyrase inhibitor. *Molecules* https://doi.org/10.3390/molecules28041593 (2023).
42. David, T. I. et al. Molecular docking analysis of phyto-constituents from *Cannabis sativa* with pfDHFR. *Bioinformation* **14**, 574–579. https://doi.org/10.6026/97320630014574 (2018).
43. Islam, S. et al. Antibacterial potential of propolis: Molecular docking, simulation and toxicity analysis. *AMB Express* **14**, 81. https://doi.org/10.1186/s13568-024-01741-0 (2024).
44. Sakhawat, A. et al. Natural compound targeting BDNF V66M variant: insights from in silico docking and molecular analysis. *AMB Express* **13**, 134 (2023).
45. Kakarala, K. K. & Jamil, K. Screening of phytochemicals against protease activated receptor 1 (PAR1), a promising target for cancer. *J. Recept. Signal Transduct. Res.* **35**, 26–45. https://doi.org/10.3109/10799893.2014.926925 (2015).
46. Mittal, L., Kumari, A., Srivastava, M., Singh, M. & Asthana, S. Identification of potential molecules against COVID-19 main protease through structure-guided virtual screening approach. *J. Biomol. Struct. Dyn.* **39**, 3662–3680. https://doi.org/10.1080/07391102.2020.1768151 (2021).
47. Daina, A., Michielin, O. & Zoete, V. SwissADME: A free web tool to evaluate pharmacokinetics, drug-likeness and medicinal chemistry friendliness of small molecules. *Sci. Rep.* **7**, 42717. https://doi.org/10.1038/srep42717 (2017).
48. Lynch, T. & Price, A. The effect of cytochrome P450 metabolism on drug response, interactions, and adverse effects. *Am. Fam. Phys.* **76**, 391–396 (2007).
49. Ullah, W. et al. Dual therapeutic potential of novel cornallegic acid: In vitro anti-inflammatory and ROS Suppression with computational insights from docking, ADMET, and DFT studies. *J. Comput. Biophys. Chem.* https://doi.org/10.1142/S2737416525500279 (2025).
50. Xiong, G. et al. ADMETlab 2.0: An integrated online platform for accurate and comprehensive predictions of ADMET properties. *Nucleic Acids Res.* **49**, W5-w14. https://doi.org/10.1093/nar/gkab255 (2021).
51. Banerjee, P., Eckert, A. O., Schrey, A. K. & Preissner, R. ProTox-II: A webserver for the prediction of toxicity of chemicals. *Nucleic Acids Res.* **46**, W257-w263. https://doi.org/10.1093/nar/gky318 (2018).
52. Alruwaili, M. et al. In silico identification and characterization of potent laccase inhibitors against *Cryptococcus neoformans*: A multi-scale computational study. *Asian J. Agric. Biol.* https://doi.org/10.35495/ajab.2024.248 (2025).
53. Ejaz, S. A. et al. In-silico Investigations of quinine and quinidine as potential Inhibitors of AKR1B1 and AKR1B10: Functional and structural characterization. *PLoS ONE* **17**, e0271602. https://doi.org/10.1371/journal.pone.0271602 (2022).
54. Rauf, A. et al. Anticancer potential of flavonoids isolated from *Pistacia chinensis* against glioblastoma (U87) cell line: Extensive in vitro and in silico research. *Eur. J. Med. Oncol.* https://doi.org/10.36922/ejmo.5768 (2025).
55. Patil, S. P. et al. Machine-learning guided discovery of bioactive inhibitors of PD1-PDL1 interaction. *Pharmaceuticals (Basel, Switzerland)* https://doi.org/10.3390/ph15050613 (2022).
56. Hamza, S. et al. 3D-QSAR, docking and molecular dynamics simulations of novel Pyrazolo-pyridazinone derivatives as covalent inhibitors of FGFR1: A scientific approach for possible anticancer agents. *J. Biomol. Struct. Dyn.* **42**, 2242–2256 (2024).
57. Shah, M. et al. Computational Analysis of ayurvedic metabolites for potential treatment of drug-resistant *Candida Auris*. *Front. Cell. Infect. Microbiol.* **15**, 1537872 (2025).
58. Friesner, R. A. et al. Glide: A new approach for rapid, accurate docking and scoring. 1. Method and assessment of docking accuracy. *J. Med. Chem.* **47**, 1739–1749. https://doi.org/10.1021/jm0306430 (2004).
59. Zhao, M. et al. Cytochrome P450 Enzymes and drug metabolism in humans. *Int. J. Mol. Sci.* https://doi.org/10.3390/ijms222312808 (2021).
60. Topalian, S. L., Drake, C. G. & Pardoll, D. M. Immune checkpoint blockade: A common denominator approach to cancer therapy. *Cancer Cell* **27**, 450–461. https://doi.org/10.1016/j.ccell.2015.03.001 (2015).
61. Javed, S. A., Najmi, A., Ahsan, W. & Zoghebi, K. Targeting PD-1/PD-L-1 immune checkpoint inhibition for cancer immunotherapy: Success and challenges. *Front. Immunol.* **15**, 1383456. https://doi.org/10.3389/fimmu.2024.1383456 (2024).
62. Wei, S. C. et al. Distinct cellular mechanisms underlie anti-CTLA-4 and anti-PD-1 checkpoint blockade. *Cell* **170**, 1120-1133.e1117. https://doi.org/10.1016/j.cell.2017.07.024 (2017).

63. Guo, J. et al. Beyond inhibition against the PD-1/PD-L1 pathway: Development of PD-L1 inhibitors targeting internalization and degradation of PD-L1. *RSC Med. Chem.* **15**, 1096–1108. https://doi.org/10.1039/d3md00636k (2024).
64. Irwin, J. J., Sterling, T., Mysinger, M. M., Bolstad, E. S. & Coleman, R. G. ZINC: a free tool to discover chemistry for biology. *J. Chem. Inf. Model* **52**, 1757–1768. https://doi.org/10.1021/ci3001277 (2012).
65. Bojarska, J. et al. A Supramolecular approach to structure-based design with a focus on synthons hierarchy in ornithine-derived ligands: Review, synthesis, experimental and in silico studies. *Molecules* https://doi.org/10.3390/molecules25051135 (2020).
66. Jankowski, K., Nowakowski, K., Grabowski, I. & Wasilewski, J. Coverage of dynamic correlation effects by density functional theory functionals: density-based analysis for neon. *J. Chem. Phys.* **130**, 164102. https://doi.org/10.1063/1.3116157 (2009).
67. RoufiedaGuerroudj, A. et al. Exploring pyrimidine-based azo dyes: Vibrational spectroscopic assignments, TD-DFT investigation, chemical reactivity, HOMO-LUMO, ELF, LOL and NCI-RDG analysis. *Spectrochim. Acta. Part A Mol. Biomol. Spectrosc.* **313**, 124093. https://doi.org/10.1016/j.saa.2024.124093 (2024).
68. Kaavin, K. et al. In-silico DFT studies and molecular docking evaluation of benzimidazo methoxy quinoline-2-one ligand and its Co, Ni, Cu and Zn complexes as potential inhibitors of Bcl-2, Caspase-3, EGFR, mTOR, and PI3K, cancer-causing proteins. *Chem. Phys. Impact* **8**, 100418 (2024).
69. Hoque, M. J., Ahsan, A. & Hossain, M. B. Molecular docking, pharmacokinetic, and DFT calculation of naproxen and its degradants. *Biomed. J. Sci. Techn. Res.* **9**, 7360–7365 (2018).
70. Ahmad, G. et al. Facile synthesis of 5-aryl-N-(pyrazin-2-yl)thiophene-2-carboxamides via suzuki cross-coupling reactions, their electronic and nonlinear optical properties through DFT calculations. *Molecules* https://doi.org/10.3390/molecules26237309 (2021).
71. Jung, J. et al. Electron transport in naphthalene diimide derivatives. *Materials (Basel, Switzerland)* https://doi.org/10.3390/ma14144026 (2021).
72. Salo-Ahen, O. M. et al. Molecular dynamics simulations in drug discovery and pharmaceutical development. *Processes* **9**, 71 (2020).
73. Habib, I. et al. Integrated computational approaches for designing potent pyrimidine-based CDK9 inhibitors: 3D-QSAR, docking, and molecular dynamics simulations. *Comput. Biol. Chem.* **108**, 108003. https://doi.org/10.1016/j.compbiolchem.2023.108003 (2024).
74. Guo, Y., Jin, Y., Wang, B. & Liu, B. Molecular mechanism of small-molecule inhibitors in blocking the PD-1/PD-L1 pathway through PD-L1 dimerization. *Int. J. Mol. Sci.* **22**, 4766 (2021).
75. Liang, J., Wang, B., Yang, Y., Liu, B. & Jin, Y. J. Approaching the dimerization mechanism of small molecule inhibitors targeting PD-L1 with molecular simulation. *Int. J. Mol. Sci.* **24**, 1280 (2023).
76. Alanzi, A., Moussa, A. Y., Mothana, R. A., Abbas, M. & Ali, I. In silico exploration of PD-L1 binding compounds: Structure-based virtual screening, molecular docking, and MD simulation. *PLoS ONE* **19**, e0306804 (2024).

Author contributions

HM, CAS and RR carried out research work and wrote the initial draft of the manuscript. MIU, HBG, and AAMA conducted the data analysis. MUK and ASA planned and supervised the study and edited the final version of the manuscript. MUK and ASA technically reviewed and finalized the draft. All authors reviewed the final version of the manuscript and approved it for publication.

Declarations

Competing interests

The authors declare no competing interests.

Additional information

Supplementary Information The online version contains supplementary material available at https://doi.org/10.1038/s41598-025-01232-7.

Correspondence and requests for materials should be addressed to M.U.K.

Reprints and permissions information is available at www.nature.com/reprints.

Publisher's Note Springer Nature remains neutral with regard to jurisdictional claims in published maps and institutional affiliations.

Publisher's note Springer Nature remains neutral with regard to jurisdictional claims in published maps and institutional affiliations.